Title: Gravity–topography regression across Antarctica: implications for isostatic regimes and subglacial crustal structure

Authors: Renata Regina Constantino[1], Kirsty Tinto[2], Leonardo Uieda[3], Carla Braitnberg[4]

[1,3] Institute of Astronomy, Geophysics and Atmospheric Sciences, University of São Paulo, SP, Brazil

[2] Lamont-Doherty Earth Observatory, Columbia University, Palisades, NY, USA

[4] Department of Mathematics, Informatics, Geosciences, University of Trieste, Italy

Email and ORCIDs:

[1] rconstantino@usp.br - 0000-0002-9025-3305

[2] tinto@ldeo.columbia.edu - 0000-0003-2558-2310

[3] uieda@usp.br - 0000-0001-6123-9515

[4] berg@units.it - 0000-0001-7277-816X

PEER REVIEW STATUS

This is a non-peer-reviewed preprint submitted to EarthArXiv.

This manuscript was submitted to Geophysical Journal International on 21 May 2026.

Abstract

We investigate the relationship between Bouguer disturbance and equivalent topography across Antarctica using satellite gravity data, under the assumption that a linear relationship is expected at long wavelengths for Airy-type isostatic compensation. Equivalent topography ensures consistency across continental, marine, and ice-covered domains by expressing bathymetry and ice loads as crustal-equivalent height. The analysis is based on the GOCO06S satellite-only gravity model and BedMachine v3 datasets. Bouguer disturbance is computed through forward modelling of all relevant mass contributions using prism integration. Spatial variations in the gravity–topography relationship are quantified using moving circular windows (264 km diameter, 75% overlap), consistent with the effective resolution of the gravity model and the wavelengths at which local compensation is expected. For each window, slope, intercept, correlation coefficient (r), coefficient of determination (R^2), and RMSE are estimated. Regions such as the Antarctic Peninsula and the southern Transantarctic Mountains exhibit high R^2 and strong negative correlation, indicating a coherent long-wavelength coupling between gravity and topography. While consistent with Airy-type compensation, this behaviour may also reflect contributions from mantle density variations associated with thermal anomalies. In contrast, large sectors of East Antarctica show positive correlation and low to moderate R^2 values. Combined with seismic evidence for thick and cold lithosphere, this pattern indicates that gravity variations are influenced by lithospheric rigidity and regional compensation rather than local Airy-type crustal thickening. The joint interpretation of regression parameters further delineates candidate subglacial sedimentary basins, in agreement with independent probabilistic models, and identifies new regions of interest for future geophysical investigation.

1. Introduction

Satellite data provide the opportunity to investigate gravity signals at continental to global scales with homogeneous resolution and coverage. Over the past two decades, major advances in mapping the Earth's gravity field have been achieved through dedicated satellite missions such as GRACE (Gravity Recovery and Climate Experiment; Tapley et al., 2004) and GOCE (Gravity field and steady-state Ocean Circulation Explorer; Rummel et al., 2011). These missions have led to the development of high-quality global gravity field models with consistent coverage, including remote regions such as Antarctica.

The long-wavelength gravity field resolved by satellite gravimetry is particularly suitable for investigating large-scale geophysical processes, including lithospheric structure, mantle convection, tectonic plate architecture, ice mass balance, and gravity variations related to climate change. Satellite observations are distributed either as gravity gradients along the satellite orbit or as global gravity field models expressed as spherical harmonic expansions (e.g., Earth Gravitational Model 2008, EGM2008; Pavlis et al., 2012; the EIGEN series, e.g., EIGEN-6C4; Förste et al., 2016; and the Gravity Observation Combination models, e.g., GOCO06S; Kvas et al., 2021). These models are provided as spherical harmonic expansions, allowing the computation of gravity disturbances or anomalies at arbitrary heights above the Earth's surface. A key advantage of global gravity field models is that the complex geodetic processing required to combine and reference satellite observations is already incorporated in the model construction, providing a stable basis for subsequent geophysical analyses.

Satellite gravity anomalies have been widely applied to investigate large-scale geodynamic processes and lithospheric structure. Applications include the assessment of tectonic domains (Ebbing et al., 2018), cross-continental correlation of geological structures (Braitenberg, 2015), recovery of lithospheric thermal structure (Pastorutti and Braitenberg, 2019), and evaluation of gravity–topography regression sensitivity on Earth and other planetary bodies (Pivetta and Braitenberg, 2020). In Antarctica, satellite gravity data have supported studies of ice mass

balance (Chen et al., 2009), ice mass transport (Rummel et al., 2011), and the derivation of lithospheric density, temperature, and viscosity structure from gravity gradients (Pappa et al., 2019). GOCE-based curvature fields have also been employed to delineate lithospheric domains and tectonic boundaries (Ebbing et al., 2018). For sedimentary basin analysis, however, investigations typically rely on higher-resolution airborne gravity surveys combined with seismic, radar, and magnetic datasets where available. Examples include the characterization of subglacial sedimentary infill in the Pensacola–Pole Basin (Paxman et al., 2019), mapping of crustal structure and sediment thickness beneath the Ross Ice Shelf (Tankersley et al., 2022), mechanical interpretation of gravity anomalies in the Ross Sea extensional basins (Karner et al., 2005), and aeromagnetic detection of structurally controlled subglacial basins in the Wilkes Subglacial Basin (Ferraccioli et al., 2009).

Geological density variations in the upper crust play a significant role in shaping the Earth's gravitational signal. This signal is not only influenced by variations in crustal thickness but also by regional differences in crustal density. According to isostatic theory (Watts, 2001), topographic loads may be compensated either locally or regionally. In local isostatic compensation, relief is balanced by variations in crustal structure: in the Airy model, topographic highs correspond to thickened crustal roots, whereas in the Pratt model compensation occurs through lateral variations in density. In contrast, regional isostatic compensation involves lithospheric flexure, in which the load is supported by the bending of an elastic plate. Flexure redistributes deformation over a broader region and produces a smooth deflection of the Moho, rather than localized changes in crustal thickness. When topographic features have sufficiently large wavelengths (~100 km), the gravitational signal mainly reflects the mass-contrast associated with the topographic load, as described by the Bouguer plate approximation. In this regime, a linear relationship is expected between the Bouguer anomaly and topography, which can be quantified through regression analysis. The regression

coefficients reflect the degree of isostatic compensation and describe the gravity–topography coupling in relation to the theoretical Airy model. Deviations from the expected linear relation may reveal crustal thickness variations, lateral density heterogeneities, or departures from local Airy-type equilibrium.

Although gravity–topography regression has been previously applied in global and planetary contexts (Braitenberg, 2015; Pivetta and Braitenberg, 2020), a systematic continent-scale assessment over Antarctica based on satellite gravity data has not yet been undertaken. Here, we apply gravity–topography regression across Antarctica to investigate the spatial variability of gravity–topography coupling. This framework enables the identification of contrasting isostatic regimes, lateral crustal density heterogeneities, and potential subglacial sedimentary basins, thereby providing new constraints on the large-scale crustal architecture of the Antarctic continent.

2. The satellite gravity data

The gravity potential field is calculated from the spherical harmonic expansion model GOCO06S (Kvas et al. 2021), part of the global satellite-only models of the GOCO*s series, which are produced by the Gravity Observation Combination (GOCO) consortium (http://www.goco.eu). The choice was based on a prior analysis done for the Antarctic continent (Scheinert et al. 2015) which concluded that the GOCO utilizes the GOCE observations in an appropriate way with minimum degradation of signals including the interior of the polar gap (which is due to the inclusion of GRACE data). The data are available at the International Centre for Global Earth Models (ICGEM, http://icgem.gfz-potsdam.de/ICGEM/, Ince et al., 2019).

The gravity disturbance grid from the GOCO06S model was obtained from the ICGEM service (http://icgem.gfz-potsdam.de/calcgrid, product "gravity_disturbance_sa") with a

129 spatial resolution of 0.6° (Fig. 1 a). In the ICGEM formulation, the disturbance grid is
130 calculated by spherical approximation on (h=0) or above (h>0) the ellipsoid. In this study, the
131 grid was calculated at a height of 5000 m to ensure that all calculations were performed above
132 the Antarctic topography. Bouguer gravity disturbance (Fig. 1b) was computed using the
133 Harmonica package (Fatiando a Terra Project, https://doi.org/10.5281/zenodo.13308312),
134 considering all relevant masses in the study area with standard density values (2670 kg/m³ for
135 crustal rocks, 1030 kg/m³ for seawater, and 917 kg/m³ for ice). The mass layers were modeled
136 over the full topographic domain, whereas the final Bouguer disturbance grid and subsequent
137 regression analysis were restricted to the region of common coverage with the satellite gravity
138 data, reducing the influence of potential edge effects. Bed topography and ice thickness were
139 taken from BedMachine Antarctica v3 (Morlighem et al., 2020) and referenced to the ellipsoid.
140 The gravity effect of eleven different mass layers (Supporting Information, Section 1),
141 referenced to the ellipsoid, was calculated using a prism approximation, and each contribution
142 was subtracted from the gravity disturbance. Technically, this subtraction product is called the
143 Bouguer disturbance, but by convention, we will refer to it as the Bouguer anomaly. Note that
144 we did not use the Bouguer anomaly grids available from ICGEM, as their formulation
145 calculates the classical Bouguer anomaly instead of the disturbance and does not account for
146 the density contrast between ice and bedrock, which is critical in ice-covered regions;
147 additionally, the water column beneath Lake Vostok was not represented as a distinct mass
148 layer in the model.

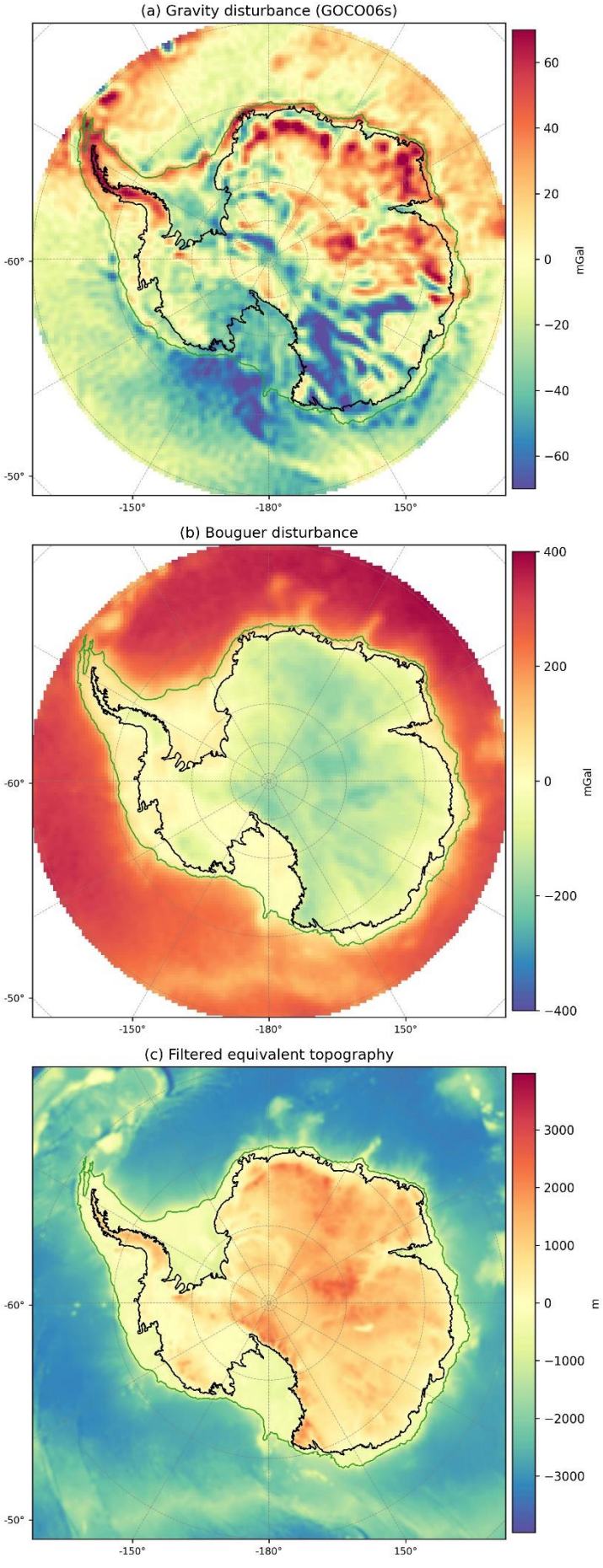
(a) Gravity disturbance (GOCO06s)
60
40
20
0
−20
−40
−60
mGal
-60°
-50°
-150°
-180°
150°
(b) Bouguer disturbance
400
200
0
−200
−400
mGal
-60°
-50°
-150°
-180°
150°
(c) Filtered equivalent topography
3000
2000
1000
0
−1000
−2000
−3000
m
-60°
-50°
-150°
-180°
150°

149

Figure 1. (a) Gravity disturbance (Kvas et al., 2021). (b) Calculated Bouguer disturbance. (c) Filtered equivalent topography. The continental shelf edge (in green) is from Amblas (2018). Grounding line from Depoorter et al., 2013.

3. Gravity regression analysis and isostatic reduction

The Bouguer correction eliminates the influence of short-wavelength topography. However, the Bouguer gravity anomaly often exhibits strongly negative values, reflecting the presence of a low-density root associated with long-wavelength topography. Recent studies have proposed statistical methods to evaluate the correlation between gravity and topographic fields (e.g., Braitenberg, 2015; Pivetta & Braitenberg, 2020). In an initial approach, these methods assume a linear relationship between the Bouguer gravity field and a filtered topography, based on the hypothesis that topography is isostatically compensated according to the Airy model. In the Airy model, topography is supported by lateral variations in the thickness of a uniform-density crust. The compensation takes the form of a crustal 'root' which projects into the mantle.

The gravity anomaly of the topography (Δg_{topo}) and of the compensation root (Δg_{root}) in the approximation of the Bouguer plate can can be defined as it follows:

$$\Delta g_{topo} = 2\pi G \rho_c H \quad (1)$$

$$\Delta g_{root} = 2\pi G (\rho_m - \rho_c) R \quad (2)$$

where G is the gravitational constant, ρ_c is the density of the crust **(**in the ideal case for topography; for bathymetry or ice-covered regions the corresponding density contrasts with water or ice should be considered), ρ_m is the density of the mantle, H is the topography while R is the compensating root. The topography and crustal root are related by

$$R = -H \frac{\rho_c}{\rho_m - \rho_c} \quad (3)$$

The gravity disturbance of an Airy model (Δg_{total}) is therefore obtained by combining the gravity effect of the topography with that of the root:

$$\Delta g_{total} = \Delta g_{topo} + \Delta g_{root}. \quad (4)$$

After applying the Bouguer correction, which removes the topographic term Δg_{topo}, the remaining contribution reflects the compensating root. Substituting Eq. (3) into Eq. (2) gives:

$$\Delta g_{root} = 2\pi G(\rho_m - \rho_c)\big(-\rho_c(-\rho_m - \rho_c)\big)H$$

$$\Delta g_{root} = -2\pi G \rho_c H \quad (5)$$

This expression (Eq. 5) shows that, in the specific case of Airy isostatic compensation, the gravitational effect of the compensating root is linearly proportional to surface topography, with proportionality factor $-2\pi G\rho_c$. In other words, once the topographic load is removed, the gravity signal reflects only the isostatic root, and its amplitude depends solely on the density of the crust and the height of the load. This constitutes the theoretical basis for interpreting Bouguer anomalies in terms of Airy-type crustal compensation.

The assumption of Airy isostasy implies that the Bouguer anomaly and filtered topography should ideally exhibit a linear relation of the form:

$$\Delta_{Bouguer} = mH_f + b \quad (6)$$

Where $m = -2\pi G\rho_c \; and \; b \approx 0$, where $\Delta_{Bouguer}$ is the Bouguer anomaly, H_f the filtered equivalent topography, m the slope, and b the intercept. A zero intercept means that 0 m of topography coincides with 0 mGal of anomaly under the Airy assumption.

By running a linear regression analysis between the Bouguer anomaly and the filtered topography, a linear anti-correlation is expected. In the absence of density heterogeneities in the crust and under conditions of Airy isostatic compensation, the slope should be equal to $-2\pi G\rho_c$. Deviations from this theoretical slope may indicate density heterogeneities (i.e. densities that are different from ρ_c and/or a crust that is isostatically under/over compensated). A non-zero intercept implies a systematic shift of the anomalies, which could be physically explained for instance by a long wavelength anomaly related to density heterogeneities in the mantle or large sedimentary basins (Pivetta & Braitenberg, 2020). In order to apply a single constant density consistently over land, ocean, and ice covered areas, an equivalent topography is used instead. The equivalent topography was computed following the rock-equivalent formulation of Hirt et al. (2012), with adaptations to explicitly account for the geometry of ice and water relative to the ellipsoidal reference surface, ensuring consistency with the layered mass representation used in the Bouguer correction. The resulting equivalent topography was then reduced in frequency content using Gaussian filter with 100 km half-transfer wavelength. This filtering step adapts the spectral content of the topography to that of the satellite-derived Bouguer field and emphasizes the long wavelengths for which the Airy approximation is expected to be most valid (Pivetta & Braitenberg, 2020).

To map the spatial variation of regression parameters across Antarctica, we applied the analysis within moving circular windows defined in metric distance. Instead of using 2° × 2° latitude–longitude boxes as in previous studies (e.g., Braitenberg, 2015; Pivetta & Braitenberg, 2020), we adopted circular windows with a diameter of 264 km and a step of 66 km (75% overlap). The window size was chosen to be compatible with the spatial scale investigated in earlier

works, while avoiding distortions introduced by angular grids in polar regions. Defining the analysis in kilometers ensures uniform spatial sampling across Antarctica, independent of longitude convergence. The 66 km step corresponds approximately to the maximum spatial resolution of the satellite gravity model (0.6°), thereby preventing artificial oversampling of the data. For each window, the linear regression was performed using ordinary least squares (OLS) with intercept. The regression was computed in two stages: first using all data points within the window; then recomputed using only points lying within 1 standard deviation from the initial regression line, in order to reduce the influence of outliers. For each window and stage, we estimated the slope, intercept, correlation coefficient, and coefficient of determination (R^2). The Pearson correlation coefficient was computed as:

$$r = \frac{\sum_{i=1}^{n}(H_{f,i}-\bar{H}_f)(\Delta Bouguer_i - \overline{\Delta Bouguer})}{\sqrt{\sum_{i=1}^{n}(H_{f,i}-\bar{H}_f)^2}\sqrt{\sum_{i=1}^{n}(\Delta Bouguer_i - \overline{\Delta Bouguer})^2}} \quad (7)$$

where n is the number of data points within the window, is the number of data points within the window, $\Delta_{Bouguer}$ is the Bouguer anomaly. The coefficient of determination was then computed as:

$$R^2 = r^2 \quad (8)$$

The regression parameters presented in the main manuscript correspond to the solution obtained after outlier removal. For comparison, maps computed using all data points (i.e., including outliers) , are provided in the Supporting Information, Section 2, as well as an interactive visualization of all individual scatter plots.

Residuals were computed within each moving window as:

$$res_i = \Delta_{Bouguer_i} - (m \cdot H_{f,i} + b) \quad (9)$$

where $\Delta_{Bouguer}$ is the Bouguer anomaly, H_f is the filtered equivalent topography, m is the estimated slope, and b is the intercept. By construction, when applying OLS with an intercept, positive and negative residuals compensate for each local regression, so that their sum equals zero. As shown in Figure S19 (Supporting Information, Section 3), the residual values associated with each regression are therefore numerically centered around zero. Their spatial pattern may highlight systematic deviations or transitions between geological domains, but their magnitude is constrained by the regression formulation.

To quantify the dispersion of the residuals within each window, we additionally computed the root mean square error (RMSE):

$$RMSE = \sqrt{\frac{1}{n}\sum_{i=1}^{n} res_i^2} \quad (10)$$

where n is the number of data points within the window. The RMSE quantifies the overall magnitude of the misfit between Bouguer anomaly and filtered topography.

Because the moving windows overlap (75% overlap), each spatial location may be associated with multiple sets of regression parameters. To construct a spatially consistent residual field, residuals are evaluated within smaller, non-overlapping square tiles (~66 km × 66 km) centered at each window location (Supporting information, Section 4. Within each tile, the residual is computed pointwise using the regression parameters derived from the corresponding circular window:

$$res\,(x,y) = Ba(x,y) - (m_{window} \cdot H_f(x,y) + b_{window}) \quad (11)$$

This spatially evaluated residual (residual map, Fig.2a) preserves the full amplitude of the misfit at each location. Unlike the residual values associated with each regression (Fig. sX

Supporting information, Section 3), which are numerically constrained by the zero-sum property of the regression, these pointwise residuals emphasize the spatial distribution and magnitude of density variations not captured by the linear gravity–topography relationship. Thus, while the regression solution enforces zero-sum residuals**,** the RMSE measures the dispersion and overall quality of the fit, and the pointwise residuals reveal the spatial amplitude of unexplained gravity signals across Antarctica.

4. Results and discussion

4.1 Residuals

The regression analysis approach is effective in distinguishing gravity signals related to deep isostatic roots from those arising from upper-crustal heterogeneities. This method assumes a linear relationship between the Bouguer gravity anomaly and suitably filtered topography, with deviations from this regression highlighted in residual maps. However, this assumption of linearity can significantly affect the interpretation of residual maps, especially in regions with steep topographies such as orogens or continental shelf edges. Non-linear effects become more pronounced in these areas, as demonstrated synthetically by Pivetta and Braitenberg (2020, their fig. 5). The steeper the topography, the stronger the artifact seen in the residual.

This effect is clearly illustrated in the residual map (Fig. 2), where the gravity high at the continental shelf break, part of an edge-effect gravity anomaly, results from the shallow density contrast between water and sediment/crust combined with the deeper mantle–crust contrast across the margin (Cochran et al., 2015, their fig. 6; Bell, 1989). Additionally, a pronounced residual high (~30 mGal) coincides with the outboard boundary of the Ross Orogeny (Grikurov et al., 2003). It is therefore crucial to interpret these results carefully, ensuring that gravity residuals associated with steep topographies are not mistakenly taken as indicators of subsurface density heterogeneity. Nevertheless, such signals can be useful in other contexts

such as fill in gaps in areas where the continental shelf edge is not fully mapped by seismic surveys.

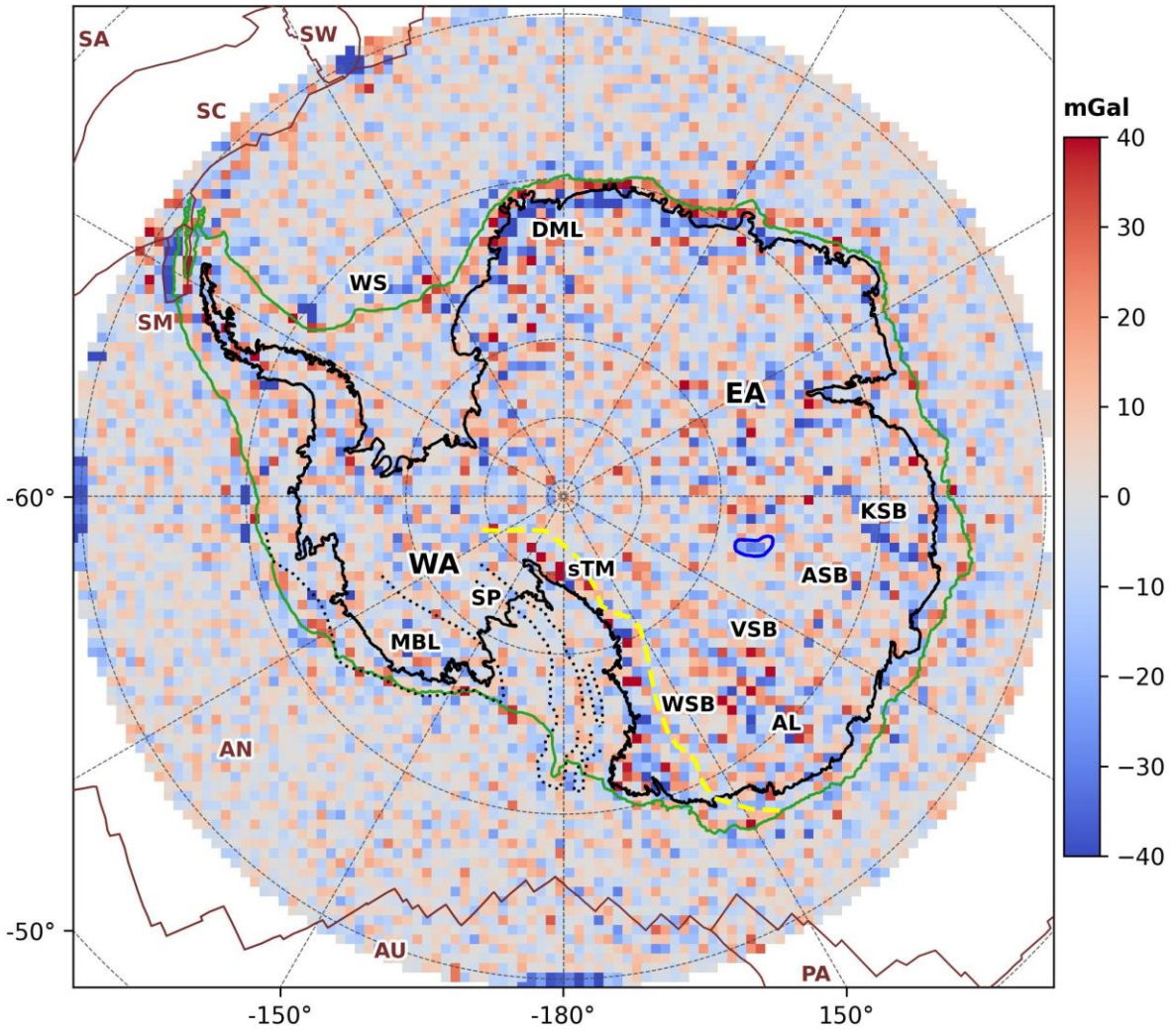

Figure 2: Regression residuals. WA = West Antarctica; EA = East Antarctica. The continental shelf edge (in green) is from Amblas (2018). LV = Lake Vostok (blue polygon); DML = Dronning Maud Land; AL = Adélie Land; KSB = Knox Subglacial Basin; VSB = Vincennes Subglacial Basin; WSB = Wilkes Subglacial basin; MBL = Marie Bird Land; SP = Siple Coast; sTM = Southern Transantarctic Mountains; WS = Weddel Sea. Tectonic plate boundaries from Bird (2003) in brown. SM = Shetland Microplate; PA = Pacific Plate; AN =Antarctic Plate; AU = Australian Plate, SC = Scotia Plate, SW = Sandwich Plate and SA = South American Plate. The Ross Orogen inboard boundary is represented by the dashed yellow line) and the Western Antarctic Rift System by the dotted black lines.

Beyond these methodological considerations, the residual map also reveals significant geological features across Antarctica. While negative anomalies (~15–20 mGal) characterize Lake Vostok, this signal is consistent with the unmodeled mass deficit associated with the

subglacial water body. The Western Antarctic Rift System (Kim et al., 2022) is marked by near-zero residual values, smoothly ranging between −2 and 2 mGal. Dronning Maud Land and Adélie Land, both described as Precambrian massifs (Kim et al., 2022), exhibit pronounced negative anomalies (< −30 mGal), although Adélie Land also displays localized positive highs surrounding these negative values. A sequence of strong negative anomalies (< −30 mGal) is further evident in the residual map; part of this signal corresponds to the Knox Subglacial Basin (Maritati et al., 2016), whereas other segments lack correlation with any currently identified geophysical features.

Furthermore, a narrow strip of negative anomalies of about −30 mGal along the margin of the Antarctic Peninsula coincides with the South Shetland Trough, which represents the northwestern boundary of the South Shetland Microplate (Bird, 2003). In contrast, the Bransfield Strait, forming the southeastern boundary of the microplate (Lawver et al., 1995), exhibits positive residual values (+3 to +7 mGal, Fig. 2a). This pattern is consistent with geophysical models indicating crustal thinning and magmatic additions within the Bransfield back-arc system (e.g., Lawver et al., 1995; Catalán et al., 2012), which may locally increase the average crustal density.

Along the Transantarctic Mountains, the residual field shows a distinct, laterally varying pattern, with alternating positive and negative anomalies that broadly track the mountain front and reflect the complex interplay between crustal structure, inherited tectonic boundaries, and flexural response. Previous studies have suggested that part of the TAM elevation, particularly in the northern and central sectors, may be supported by a crustal root (e.g., Studinger et al., 2004; van Wijk et al., 2008). However, more recent seismic studies indicate that such a root, if present, is not a continuous along-strike feature (Hansen et al., 2016). In our residuals, there is no clear evidence of distinctive regimes along the TAM.

In addition to the spatial distribution of residuals, the root mean square error (RMSE) (Fig. 3) provides a complementary measure of the dispersion of the gravity–topography relationship within each regression window. Whereas individual residuals represent the deviation between observed and predicted Bouguer anomaly values, the RMSE summarizes the typical magnitude of this misfit and therefore provides a spatial measure of how closely the gravity field follows the linear relationship assumed in the regression model.

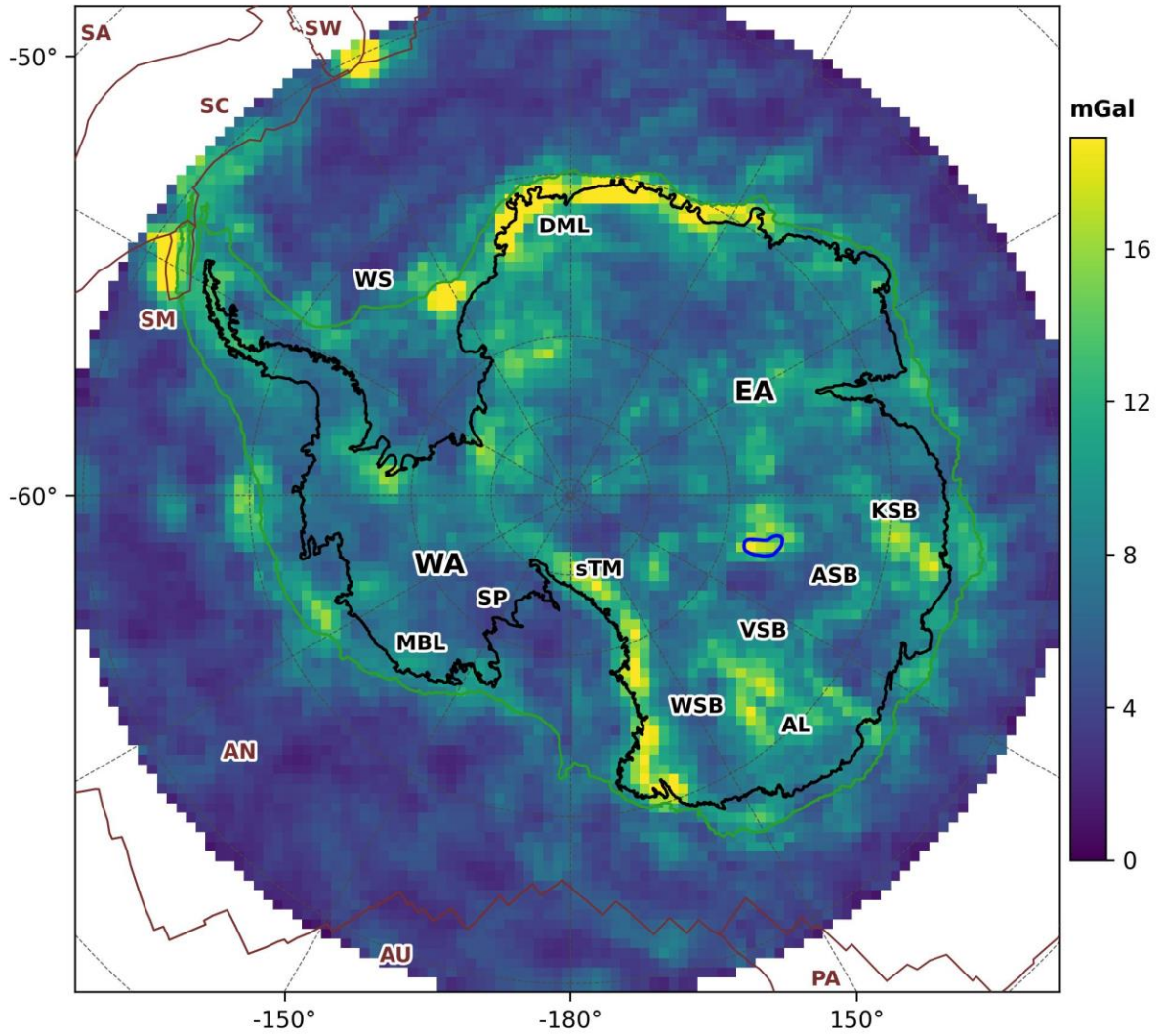

Figure 3: Root Mean Square Error. Abbreviations of geological features are the same as in Fig. 2.

The RMSE map (Fig. 3) highlights regions where the Bouguer–topography relationship departs from the ideal linear behavior assumed in the regression model. Low RMSE values (< ~6 mGal)

indicate areas where the Bouguer anomaly closely follows the gravity predicted from filtered topography, reflecting a coherent gravity–topography relationship consistent with the gravity effect of the compensating crustal root associated with surface topography. Such behavior is observed over the Antarctic Peninsula, Marie Byrd Land, and large portions of the continental shelf.

In contrast, elevated RMSE values occur in several sectors of Antarctica, indicating stronger dispersion of the gravity–topography relationship. In some regions, such as Lake Vostok, the Knox Subglacial Basin, and parts of Adélie Land, high RMSE values suggest that localized density variations or sedimentary basins introduce gravity signals that are not fully described by the regression model.

A different behavior is observed along the Transantarctic Mountains, where RMSE values are also relatively high. In this region, the dispersion likely reflects the large topographic gradients of the orogenic belt and the complex interplay between crustal thickness variations, flexural support of the mountain range, and thermal anomalies in the lithospheric mantle. These factors can locally perturb the gravity–topography relationship and increase the dispersion of the regression.

Elevated RMSE values are also observed in parts of Dronning Maud Land, particularly near the transition between the continental interior and the continental margin. Geological compilations (e.g., Kim et al., 2022) indicate that this sector comprises a complex assemblage of Jurassic–Cretaceous volcanic margins superimposed on Archean massifs and Neoproterozoic platformal crust. Such lithospheric heterogeneity likely produces strong lateral density contrasts associated with magmatic intrusions, volcanic sequences, and transitional crustal domains, which increase the dispersion of the gravity–topography relationship. The implications of these patterns are further explored in the following sections through the combined analysis of the regression parameters.

For completeness, the map of mean residual values associated with each regression (Fig. SX, Supporting Information, Section 3) shows values numerically centered around zero across the study area, with regional differences confined to variations at approximately the thirteenth decimal place. West Antarctica and the continental shelf exhibit values effectively equal to zero within numerical precision, whereas East Antarctica shows slightly greater spatial variability, with differences on the order of 10^{-13}. Despite their small magnitude, this spatial pattern is consistent with the first-order geological distinction between the two provinces: West Antarctica is characterized by thinner and tectonically active crust (e.g., Chaput et al., 2014; Ji et al., 2022), whereas East Antarctica corresponds to the more stable East Antarctic craton (e.g., Baranov & Morelli, 2013; Llubés et al., 2018).

4.2 Correlation coefficient map

From the assumptions of the method, which considers the crust to be in local Airy isostatic equilibrium, a linear anti-correlation between the filtered equivalent topography and the Bouguer anomaly is expected (Turcotte & Schubert, 2002). However, results reveal several regions where a positive correlation is observed (Fig. 4). Such behavior indicates departures from classical isostasy and may suggest undercompensation or the presence of local mass anomalies not accounted for by the Airy model. Undercompensation may occur where elevated topography is not fully supported by a compensating crustal root, producing Bouguer anomalies that are less negative than expected for complete isostatic balance (Watts, 2001). In such cases, gravity and topography vary in the same sense rather than reflecting a fully compensating crustal root. In addition to undercompensation, positive gravity–topography correlations may also reflect subsurface density heterogeneities within the crust or upper mantle, which contribute to the gravity signal beyond the assumptions of local Airy compensation (e.g. Simons et al., 1994; Watts, 2001).

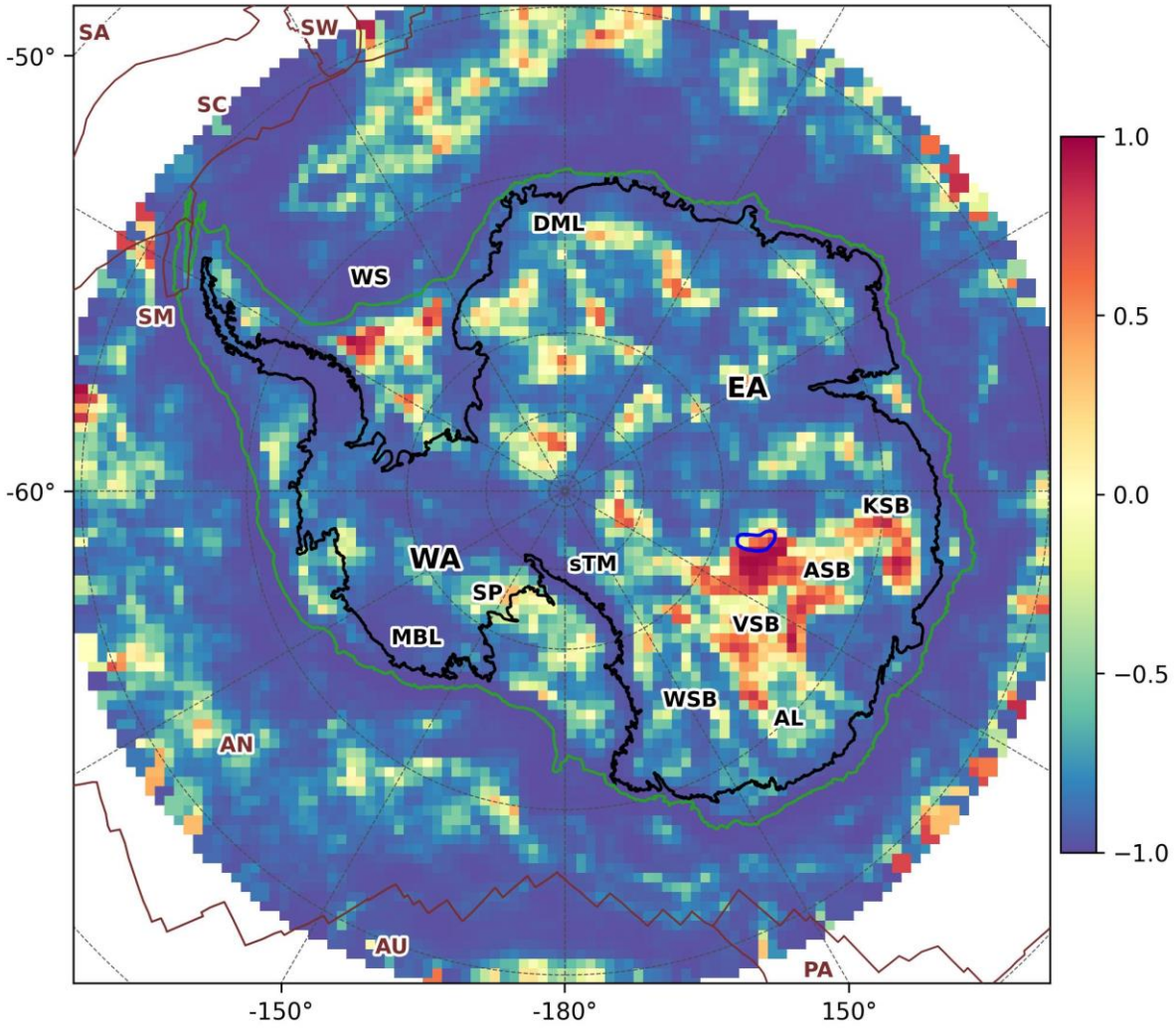

Figure 4. Correlation coefficient between Bouguer anomaly and filtered equivalent topography. Abbreviations of geological features are the same as in Fig. 2.

Positive Bouguer–topography correlations display a clear spatial organization. Over the Antarctic continent, they occur predominantly in East Antarctica, with only one limited exception near the transition between the continental interior and the Ross Ice Shelf at Siple Coast. In the surrounding oceanic domain, two additional sectors stand out: one adjacent to the Shetland microplate near the northern Antarctic Peninsula, and another close to the continental shelf break in the Weddell Sea. Within East Antarctica, all regions exhibiting positive correlation are located where S-wave velocities range between 4.5 and 4.6 km s^{-1} at depths of

417 approximately 100–150 km (An et al., 2015). The association between positive correlation and
418 high-velocity lithospheric over an old and cold lithosphere favors flexural support rather than
419 local isostatic control.
420 Variations in ice mass could also influence the Bouguer–topography relationship by
421 introducing a mismatch between the surface load represented in topographic models and the
422 gravitational field used in the regression. Changes in ice load generate an instantaneous elastic
423 response of the lithosphere, whereas the viscoelastic adjustment of the mantle evolves over
424 much longer timescales, from decades to millennia, following major glacial loading changes
425 (Peltier, 2004; Berg et al., 2024). Consequently, gravity and surface elevation may reflect
426 responses to ice loading acting on different timescales. In this study, the equivalent-topography
427 field incorporates a static representation of ice thickness from the BedMachine Antarctica
428 dataset (Morlighem et al., 2020), whereas the Bouguer anomalies are derived from the static
429 component of the GOCO06s gravity model, representing the mean gravity disturbance over the
430 period 2002–2016 (Kvas et al., 2021). Importantly, BedMachine does not represent a snapshot
431 of ice conditions over the GOCO06s averaging interval. Instead, it integrates multiple
432 observational datasets, including radar and altimetry, many of which postdate 2016. Any
433 mismatch between the ice distribution represented in BedMachine and the mean ice load
434 contributing to the gravity field over 2002–2016 may therefore leave a residual ice-related
435 signal in the Bouguer anomaly, potentially affecting the Bouguer–topography relationship at a
436 regional scale. However, satellite altimetry observations indicate that, although significant ice
437 mass losses occurred along coastal sectors of Greenland and West Antarctica between 2003
438 and 2019, ice-thickness changes over the interior of Antarctica, where positive Bouguer,
439 topography correlations are predominantly observed, were small, typically below 0.15 m yr^{-1}
440 (Smith, et al. 2020). Even considering potential temporal inconsistencies between the gravity
441 field (averaged over 2002–2016) and the ice-thickness data incorporated in BedMachine, the

resulting difference in ice load between the respective acquisition periods would amount to at most a few meters of ice. The associated gravity effect (~0.1 mGal) is negligible relative to gravity variations of crustal-scale magnitude (tens of mGal). Such temporal mismatches may introduce minor residual signals, but their magnitude is insufficient to account for the observed positive gravity–topography correlations, which more likely reflect deviations from local Airy equilibrium or lateral density heterogeneities within the crust.

In the oceanic domain, the positive correlation observed near the continental shelf break in the Weddell Sea may reflect uncertainties associated with poorly constrained bathymetry, which can affect both the Bouguer correction and the equivalent-topography calculation in transitional continental–oceanic settings. In addition, a band of positive correlation observed southwest of the South Shetland microplate, within the Antarctic Plate, likely reflects localized lithospheric heterogeneity rather than large-scale crustal-thickness variations. Its linear geometry is consistent with structural inheritance associated with the former Phoenix–Antarctic convergent margin and with tectonic segmentation of the South Shetland microplate (Taylor et al., 2008). Such inherited tectonic processes may have produced localized compositional and density heterogeneities within the crust, so that bathymetric relief is spatially associated with higher-density material, generating gravity variations that correlate positively with topography. Conversely, negative correlations dominate much of the continental interior (Fig. 4), where high topography corresponds to low Bouguer anomalies under near-Airy compensation.

When the correlation and residual fields are examined together, distinct regional behaviors emerge across Antarctica. Both Dronning Maud Land and the Transantarctic Mountains exhibit strong negative correlations ($r \approx -0.8$ to -1), indicating that topography and Bouguer gravity vary inversely, consistent with compensation dominated by variations in crustal thickness. However, the residuals reveal contrasting mass distributions. In Dronning Maud Land, negative residuals indicate that the observed Bouguer anomaly is lower than predicted, suggesting a

local mass deficit and nearly complete compensation or slight overcompensation. In contrast, along the Transantarctic Mountains the Bouguer–topography correlation remains predominantly strong and negative over most of the range. Superimposed on this first-order pattern, the residual field displays both positive and negative values distributed along strike, without a clear spatial organization or systematic correspondence with the correlation map. When examined together with the residual field, the regions previously identified as exhibiting positive correlation reveal distinct second-order mass distributions superimposed on this regional compensation regime. Over the Lake Vostok region, the Knox Subglacial Basin, Adventure Subglacial Basin, and Vincennes Subglacial Basin, all located within the East Antarctic sector characterized by positive correlation and high lithospheric velocities, present negative residuals (≈ −20 to −25 mGal), indicating areas with localized subglacial zones filled with low-density material (negative residuals) superimposed on a regional Bouguer–topography relationship that departs from local Airy-type compensation. In contrast, a north–south-oriented band west of the Shetland microplate exhibits positive correlations associated with positive residuals, suggesting the presence of higher-density material or compositional heterogeneities within the crust. This behavior is compatible with the influence of lateral density heterogeneities or other non-Airy compensating mechanisms, potentially related to structural complexities near the transition between continental and oceanic crust. Adélie Land exhibits both positive and negative correlation values, accompanied by residuals of varying sign, indicating spatially variable mass distributions. This heterogeneous pattern contrasts with the more coherent domains described elsewhere and reflects the complex polyphase tectonic evolution of the region (Naumenko-Dèzes et al., 2020; Harley, 2014; Gapais et al., 2008). In such structurally heterogeneous crust, lateral density contrasts may locally influence the gravity–topography relationship, producing behavior that approaches a Pratt-type response without implying a distinct large-scale compensation regime.

A comparison between the correlation and RMSE maps further clarifies the nature of the gravity–topography relationship in these regions. Within the East Antarctic domain previously identified as exhibiting positive Bouguer–topography correlation and S-wave velocities between 4.5 and 4.6 km s^{-1} at depths of approximately 100–150 km (An et al., 2015), several localized regions display elevated RMSE values. These include Lake Vostok, the Vincennes Subglacial Basin, the Knox Subglacial Basin, and Adélie Land, where elevated RMSE values indicate localized departures from the regional gravity–topography relationship, likely related to sedimentary basin infill, subglacial lakes, or lateral crustal density contrasts. Parts of the Weddell Sea continental shelf edge also exhibit positive correlation associated with high RMSE values, which may reflect uncertainties related to poorly constrained bathymetry in transitional continental–oceanic settings.

Despite these localized departures, the largest continuous area characterized by positive Bouguer–topography correlation (Fig. 4) presents relatively low RMSE values (< 6 mGal). When analyzed together with the S-wave velocity structure at greater depth (An et al., 2015, their fig. 6d), this region coincides with the domain of maximum lithospheric S-wave velocities at approximately 200 km depth. The combination of positive correlation and low RMSE therefore indicates that the gravity–topography relationship in this sector remains largely linear, suggesting a coherent regional signal that may reflect the mechanical influence of a strong and rigid lithosphere rather than purely local Airy-type crustal compensation.

4.3 R-Squared map

In analyzing the relationship between Bouguer anomaly and the filtered topography, the R-squared (R^2) value (Fig. 5) indicates how well the variation in topographic features explains the variation in gravity anomalies. Under the assumptions of the method, high R^2 values are compatible with behavior consistent with Airy-type isostatic equilibrium in the lithosphere

(Watts, 2001), as the Bouguer anomaly varies consistently with the crustal root inferred from topography.

Conversely, low R^2 values (e.g., Wilkes Land, Coats Land, and parts of the Weddell sector; Fig. 5) indicate that the relationship between the Bouguer anomaly and the crustal root inferred from topography departs from that expected under Airy-type compensation. Such values may reflect alternative modes of isostatic compensation, such as Pratt-type compensation or flexural behavior, as well as subsurface mass anomalies or vertical variations in lithospheric structure not captured by the Airy model. In these regions, the deviations likely arise from a combination of isostatic and non-isostatic processes.

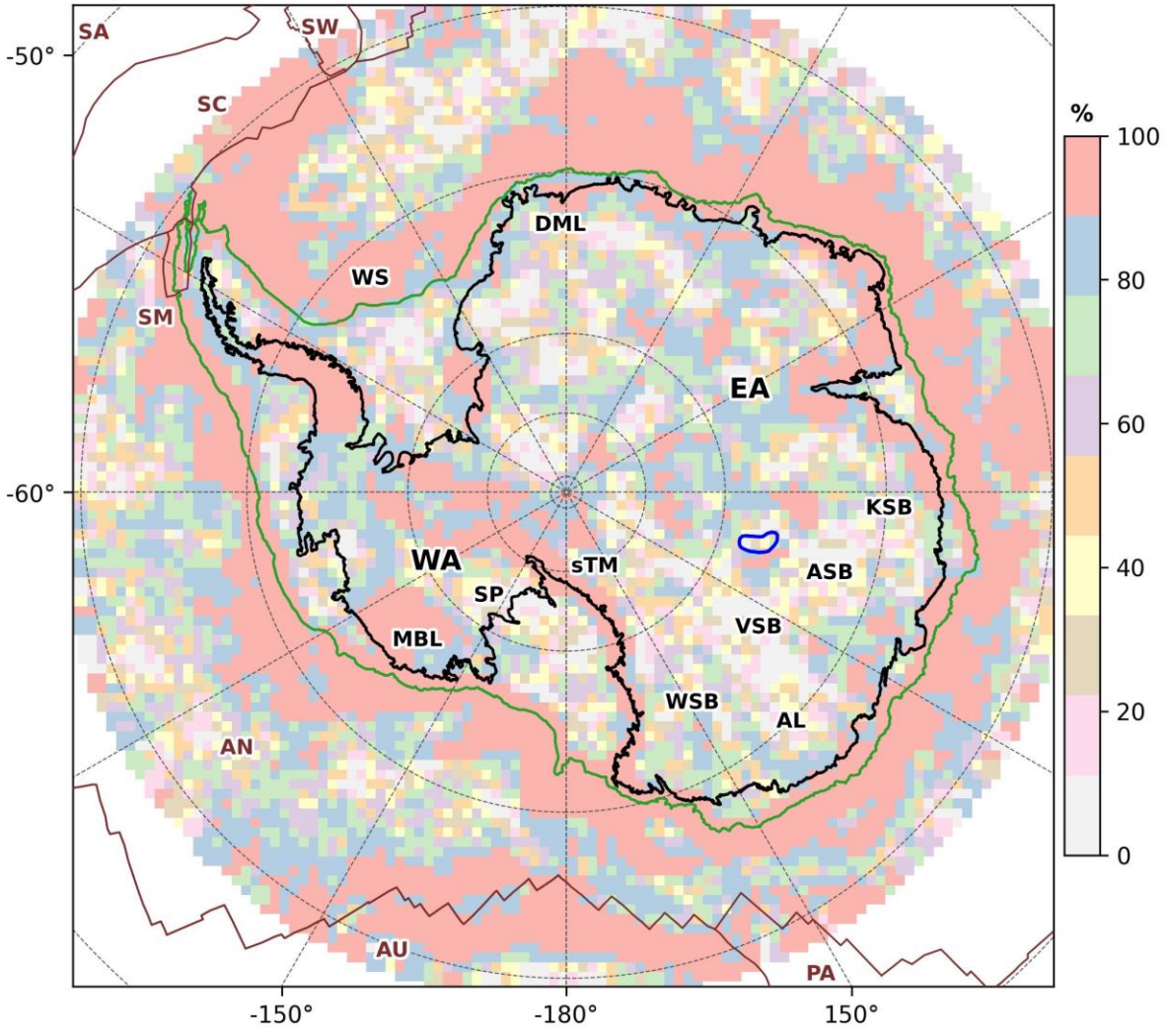

Figure 5. Coefficient of determination (R^2). Abbreviations of geological features are the same as in Fig. 2.

Surrounding the Transantarctic Mountains, particularly in the southern sector, high R^2 values (>90%; Fig. 5) indicate that the Bouguer anomaly is strongly explained by the equivalent root predicted from topography within the adopted Airy framework. However, independent geophysical studies suggest that the Transantarctic Mountains may not be in classical local Airy isostatic equilibrium (e.g. Stern and ten Brink, 1989; Wannamaker et al. 2017; Shen et al. 2018). This apparent contradiction implies that the mass distribution responsible for the gravity–topography relationship may not correspond to a purely crustal root, but instead to deeper sources producing an equivalent gravimetric effect. Thermal anomalies and density reductions in the lithospheric mantle, as indicated by slow uppermost mantle velocities (Shen et al., 2018), may provide buoyant support to the range. Elevated temperatures in the uppermost 60–100 km of the mantle can reduce mantle density by approximately 1–1.5%, generating a mass deficit comparable to that expected from crustal thickening and thereby reproducing a gravity signal statistically consistent with an Airy-type root.

A high R^2 value (greater than 85%, Fig. 5) is also observed along the Antarctic Peninsula. In this region, previous seismic studies have identified slow shear-wave velocities in the upper mantle associated with the formation of a slab window produced by the subduction of the Phoenix–Antarctic spreading center (Lloyd et al., 2020). This tectonic configuration allowed hot asthenospheric material to rise beneath the peninsula, replacing portions of the pre-existing lithosphere and generating thermal anomalies in the upper mantle. Tomographic models indicate that these slow velocities reflect warm mantle material beneath the Pacific margin of the Antarctic Peninsula, where the subduction of successive ridge segments progressively modified the lithospheric structure (Lloyd et al., 2020). Such thermally altered mantle may influence the gravity–topography relationship by producing density variations beneath the crust.

A similarly high R^2 value is observed over Marie Byrd Land, where pronounced slow wave-speed anomalies extend through the upper mantle. Seismic tomography shows that these slow anomalies extend from depths of approximately 75 km to about 200–250 km and may continue into the transition zone beneath parts of West Antarctica, although their deeper extent remains uncertain (Lloyd et al., 2020). These observations are commonly interpreted as evidence of elevated mantle temperatures beneath the region and have been linked to the presence of a mantle plume or plume-like thermal anomaly (LeMasurier and Landis, 1996; Lloyd et al., 2020). Geological observations further indicate that uplift of the Marie Byrd Land dome occurred broadly contemporaneously with the onset of widespread volcanism around 28–30 Ma, suggesting a close relationship between mantle thermal processes, magmatism, and regional uplift (LeMasurier and Landis, 1996). Elevated mantle temperatures and associated density reductions may therefore contribute to the gravity–topography correspondence observed in this region.

Over the continental shelf, high R^2 values result from the predictable isostatic compensation of the oceanic lithosphere. The thinner and more uniform lithosphere along continental margins facilitates a clear correlation between gravity anomalies and surface topography. Additionally, in continental shelf settings, sedimentary basins can contribute to high R^2 values, as laterally extensive, low-density sedimentary loads produce gravity responses that are systematically related to surface and subsurface topography (Cochran, 1979). Consequently, the homogeneous nature of the oceanic lithosphere, combined with isostatic adjustments to sediment loading, leads to significant R^2 values, reflecting a strong linear relationship between Bouguer gravity anomalies and topography.

When the R^2, correlation, and residual maps are examined together, a coherent pattern emerges linking the gravity–topography fit to the underlying compensation regime. Regions such as the Antarctic Peninsula, Marie Byrd Land, and the Southern Transantarctic Mountains display high

R^2 values (> 80%), strong negative correlation, and residuals near zero. This combination indicates a stable long-wavelength coupling between gravity and topography that is compatible with the assumptions of Airy-type isostatic compensation. However, as highlighted by mantle seismic studies (e.g., Shen et al., 2018; Lloyd et al., 2020), such a strong linear relationship may also result from deeper processes, including thermally induced density reductions or coupling within the lithosphere. In these areas, the statistical relation between gravity and topography reflects the effectiveness of large-scale compensating mechanisms rather than purely Airy isostasy.

In contrast, regions such as Lake Vostok (e.g. Carter et al,. 2007), the Knox Subglacial Basin, the Adventure Subglacial Basin, and the Vincennes Subglacial Basin (e.g. Aitken et al., 2014) combine positive Bouguer–topography correlations with negative residuals and display low R^2 values (<30%), indicating that topography explains only a small fraction of the Bouguer anomaly variance in these areas. At Lake Vostok, the negative residuals are consistent with the presence of a subglacial water body, which produces a localized mass deficit relative to the surrounding crust superimposed on a gravity–topography relationship dominated by localized density contrasts in the upper crust (e.g., subglacial water and sedimentary infill), rather than by variations in crustal thickness predicted by local Airy-type compensation**.** In the Knox, Adventure, and Vincennes subglacial basins, a similar regression pattern is consistent with fault-bounded sedimentary basins containing several kilometers of relatively low-density sedimentary fill**,** as indicated by their low gravity signature, smooth magnetic character, and large depth to magnetic basement (Aitken et al., 2014). These basins reflect the underlying tectonic architecture of the East Antarctic crust and represent subglacial depressions developed within a regional support regime rather than local Airy-type isostatic compensation. Strongly negative residuals also characterize Dronning Maud Land and Adélie Land, where correlation remains dominantly negative but spatially variable and R^2 tends to be moderate, consistent with

heterogeneous crustal structure and lateral density variations. The Transantarctic Mountains, marked by some positive residuals and moderate to high R^2 values, represent a distinct regime in which the gravity field and topography are coherently related but supported by thermal rather than purely isostatic processes.

Taken together, these relationships indicate that R^2, correlation, and residuals must be interpreted jointly: high R^2 and strong anti-correlation may denote stable long-wavelength coupling between gravity and topography, whether driven by coherent thermal responses or by classical Airy-type compensation, whereas low to moderate R^2 values combined with positive correlation or large residuals highlight regions where the gravity–topography relation departs from isostatic behavior, reflecting lateral density contrasts, thermal anomalies, or localized lithospheric heterogeneity.

Across East Antarctica, areas of maximum positive correlation are commonly associated with low coefficients of determination (R^2), indicating that Bouguer anomaly and equivalent topography vary in the same direction, but their relationship is not explained by a simple Airy-type linear compensation model. A notable exception occurs between 90°E and 120°E, where the correlation reaches its highest values and the inferred R^2 is strongly sensitive to outlier treatment. In this sector, R^2 is high (~80%) when the regression is recomputed after excluding points beyond one standard deviation of the initial fit, but drops to <10% when all data points are retained (Supporting Information, Section 2). This behavior suggests that the Bouguer–topography relationship in this region is not governed by a single process. Instead, the dataset appears to contain a dominant linear component together with a subset of data points that systematically depart from it. Excluding these values reduces their influence on the regression and stabilizes the estimate of the dominant gravity–topography relationship. Such departures typically occur where the linear assumption is locally violated, for example in areas of strong topographic gradients such as continental margins or shelf breaks, where non-linear effects

become significant. These departures may reflect lateral density heterogeneities within the crust, such as compositional variations or intrusive bodies, which introduce additional mass contributions not accounted for by a simple Airy-type model. Such complexity is consistent with a compensation regime that departs from local isostatic equilibrium, potentially involving flexural support and lateral variations in lithospheric rigidity.

When R^2 is examined together with RMSE, two contrasting behaviors emerge across Antarctica. In regions such as the Transantarctic Mountains, Dronning Maud Land, and the Shetland Microplate, R^2 values exceed 80%, indicating a strong regional gravity–topography relationship, while RMSE values remain high (> 14 mGal), reflecting substantial dispersion around the regression. In the Transantarctic Mountains, this dispersion likely reflects the combined influence of large topographic gradients, flexural support of the range, and thermal anomalies within the lithosphere and upper mantle. In Dronning Maud Land, the high dispersion occurs near the transition between the continental interior and the continental margin, where Jurassic–Cretaceous volcanic margins are superimposed on Archean massifs and Neoproterozoic platformal crust (Kim et al., 2022). Such lithospheric heterogeneity likely produces strong lateral density contrasts associated with magmatic intrusions, volcanic sequences, and transitional crustal domains. A comparable effect may occur in the Shetland Microplate, where lithospheric fragmentation and complex tectonic interactions introduce additional density contrasts that affect the gravity field (Taylor et al., 2008).

In contrast, regions such as Lake Vostok, the Knox Subglacial Basin, and Adélie Land are characterized by low R^2 values, predominantly below 20%, and high RMSE values (> 14 mGal). In these areas, the Bouguer anomaly variance is only weakly explained by the regression, indicating that localized density contrasts dominate the gravity field. At Lake Vostok, the presence of a large subglacial water body produces a significant mass deficit relative to the surrounding crust (e.g., Carter et al., 2007). In the Knox Subglacial Basin and

Adélie Land, the gravity field likely reflects fault-bounded basins containing several kilometers of low-density sedimentary fill and complex crustal structure (e.g., Aitken et al., 2014).

4.4 Intercept map

In isostatic models, a zero intercept indicates that a topography of 0 m corresponds to a Bouguer anomaly of 0 mGal. In contrast, a non-zero intercept reflects a systematic offset of the Bouguer field relative to the reference level defined by zero topography. Within the regression framework described in Eq. (6), the intercept therefore represents a constant shift of the Bouguer anomaly relative to the level predicted from topography alone. Under ideal Airy isostatic compensation this value should remain close to zero, whereas deviations from zero indicate the presence of mass contributions that are not accounted for by the Airy-based gravity–topography relationship. Such offsets may arise from long-wavelength density variations within the mantle or from large sedimentary basins (Pivetta and Braitenberg, 2020). In addition, Pivetta and Braitenberg (2020) show that non-zero intercepts may also appear in synthetic models due to nonlinear effects not accounted for in the regression, typically remaining below 10 mGal, and the authors say that this may occur in oceanic regions characterized by extensive abyssal plains where topography varies little over large areas.

The intercept values for Antarctica (Fig. 6) are predominantly negative in East Antarctica (EA) and positive in West Antarctica (WA), which may be associated with the long-wavelength component of the Moho, shallower in WA (~25 km) and deeper in EA (> 40 km) (An et al., 2015). Such a first-order pattern suggests that the intercept partly reflects large-scale lithospheric structure across the Antarctic continent. The most significant negative intercepts within the continental interior occur in East Antarctica, where they coincide with regions of positive Bouguer–topography correlation. This combination suggests that the signal is not consistent with low-density sedimentary infill, which would be expected to generate negative

Bouguer anomalies and a negative correlation with topography. Instead, the observed positive correlation combined with a negative intercept points to the presence of relatively shallow, dense crustal structures or incomplete isostatic compensation. Such structures may include basins containing relatively dense lithologies, such as volcanic intrusions, high-density evaporitic layers (e.g., anhydrite), or, in some cases, relatively dense carbonate rocks (e.g., dolomite), which may locally exceed average crustal densities. Such structures may include basins containing relatively dense lithologies, such as volcanic intrusions, high-density evaporitic layers (e.g., anhydrite), or, in some cases, relatively dense carbonate rocks (e.g., dolomite), which may locally exceed average crustal densities. Although positive Bouguer anomalies have been documented in several sedimentary basins worldwide (e.g., North Park Basin, Colorado – Behrendt and Popenoe, 1969; Mediterranean Basin – Morelli, 1990; Ross Sea – Karner et al., 2005), such anomalies do not necessarily imply a non-zero intercept, highlighting that the gravity–basin relationship is not straightforward. Among these examples, the Ross Sea represents the only well-studied Antarctic case (Karner et al., 2005), providing a useful reference for comparison.

The Ross Sea basins display negative intercepts associated with negative Bouguer–topography correlation. This behavior has been explained by deep-seated, laterally extensive density contrasts related to rifting and crustal thinning, which dominate the gravity signal independently of surface elevation (Karner et al., 2005). In contrast, areas of East Antarctica characterized by positive Bouguer–topography correlation combined with negative intercepts may indicate that gravity increases with elevation while the overall Bouguer level remains systematically lower than predicted by the regression. This configuration is consistent with the presence of relatively shallow, dense crustal structures that contribute to the gravity field but are not fully balanced by a corresponding crustal root, resulting in a departure from complete Airy-type compensation. In this context, the negative intercept reflects a systematic downward

shift of the Bouguer field relative to the Bouguer anomaly expected from the gravity–topography relationship**,** indicating a mismatch between surface topography and the depth or magnitude of the compensating mass. Together, these contrasting behaviors suggest that parts of East Antarctica may be influenced by shallow, localized dense bodies superimposed on a broadly compensated lithosphere, whereas in the Ross Sea the gravity field reflects deeper, laterally distributed mass contributions that are largely decoupled from surface topography. More generally, the intercept captures regional mass contributions that are not accounted for by the gravity–topography relationship, reflecting long-wavelength lithospheric density variations that are not represented in the topographic load.

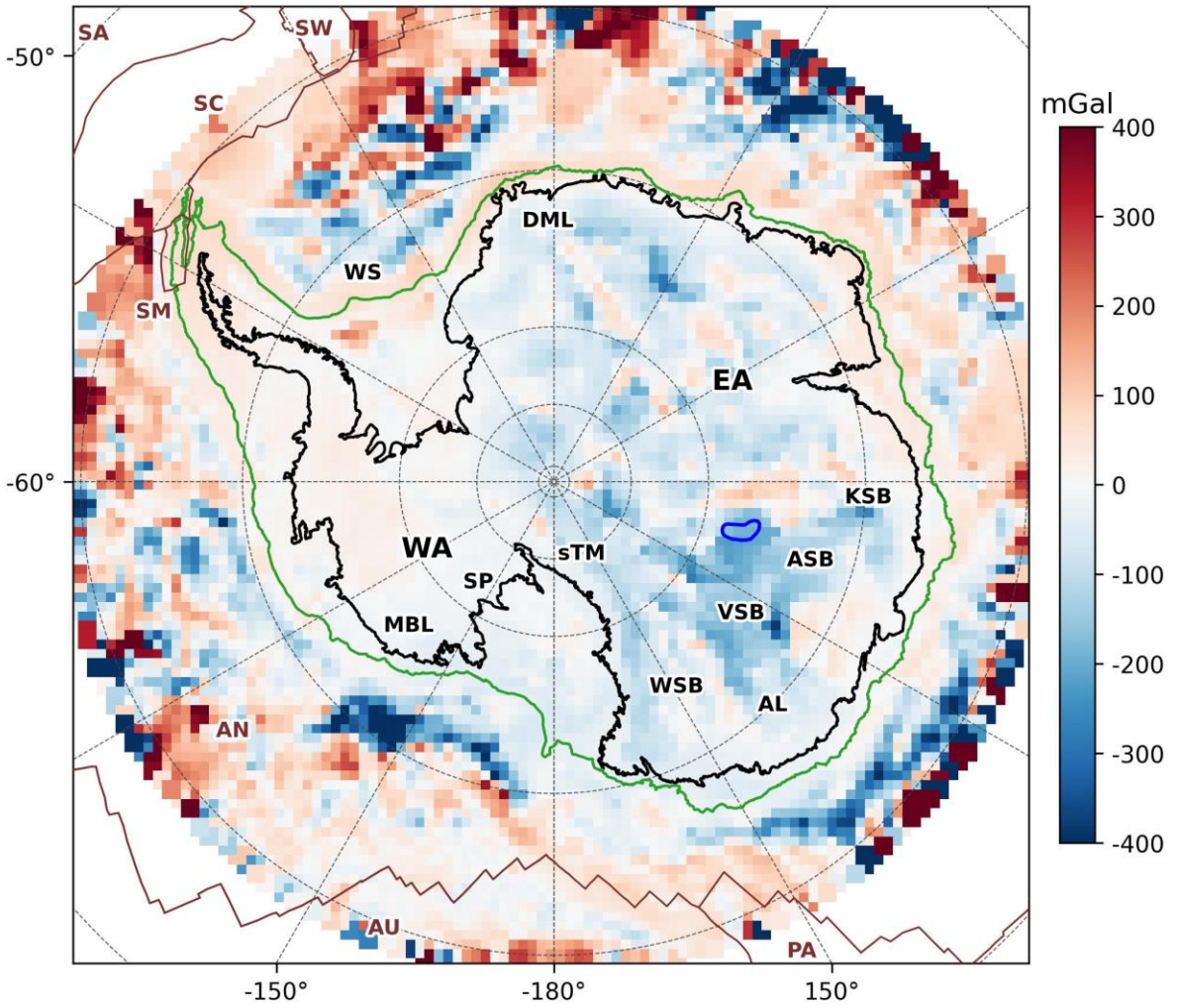

Figure 5. Intercept map showing the spatial distribution of regression intercepts between Bouguer anomaly and filtered topography. Abbreviations of geological features are the same as in Fig. 2.

These differences are also reflected in their magnetic signatures. Most regions characterized by strongly negative intercepts (approximately −150 to −200 mGal, Fig. 6) and positive Bouguer–topography correlation (Fig. 2) do not coincide, in the ADMAP2 dataset (Golynsky et al., 2018, (Figure SX, Supporting information, Section 5), with areas exhibiting low-amplitude, laterally smooth magnetic anomalies resulting from attenuation of the basement magnetic signal, as expected for sedimentary basins characterized primarily by low-magnetization sedimentary fill and a laterally uniform basement response (Telford et al., 1990; Blakely, 1995; Hinze et al., 2013). Therefore, these intercept minima are more consistent with the coexistence of density and magnetization contrasts within the crust. Such signatures may reflect domains containing dense and compositionally diverse lithologies, potentially related to the long-term crustal evolution of East Antarctica through multiple tectonic and magmatic episodes that produced a structurally and compositionally heterogeneous continental interior.

In contrast, the Ross Sea is characterized by a distinct magnetic behavior that does not directly delineate the sedimentary basins identified by Karner et al. (2005). In regions where intercept values range between 0 and −20 mGal, the magnetic field is dominated by smooth, predominantly negative anomalies, mainly beneath the Ross Ice Shelf. More negative intercepts (approximately −20 to −60 mGal) are associated with increased magnetic complexity, characterized by high-frequency positive and negative anomalies. Although the Ross Sea basins described by Karner et al. (2005) fall within this latter intercept range, neither the magnetic patterns nor the intercept contours provide a clear geometric definition of the basin architecture. This lack of direct correspondence suggests that the magnetic signal in the Ross Sea is not primarily controlled by the sedimentary basins themselves, but instead reflects a more complex crustal and lithospheric structure.

In East Antarctica, particularly across Wilkes Land and Coats Land, strongly negative intercepts coincide with low R^2 values (Fig. 5), indicating the presence of a pronounced

744 regional gravity offset that is not accounted for by local Airy-type isostatic compensation. Such
745 large negative intercepts indicate that the Bouguer field is systematically shifted toward lower
746 values relative to the level predicted from topography alone, implying the presence of
747 additional mass contributions independent of surface relief. In these regions, gravity variations
748 are therefore dominated by a regional gravity offset controlled by deep-seated density contrasts
749 rather than by topography-driven isostatic responses.
750 A similar pattern is observed in the Weddell Sea sector, where the limited quality of
751 bathymetric control may further degrade the gravity–topography regression and reduce R^2
752 values. Taken together, the combination of strongly negative intercepts and low R^2 values
753 indicates the coexistence of a pronounced long-wavelength gravity offset, consistent with deep-
754 seated density contrasts, and a gravity–topography relationship that is not governed by local
755 Airy-type isostatic compensation, potentially reflecting Pratt-type or flexural isostatic
756 behavior, or the absence of isostatic equilibrium.
757
758 **4.5 Slope map**
759 According to the assumptions of the method (Eq. 6), the regression slope should approach the
760 theoretical value $-2\pi G\rho c$ (i.e. -0.1123 mGal m^{-1} when assuming an average crustal density of
761 2.67 g cm^{-3}). Although the regression slope may be influenced by the frequency content of the
762 topography, the equivalent topography was filtered to minimize this effect (Pivetta &
763 Braitenberg, 2020). Figure 6 shows that the slope values deviate significantly from the
764 theoretical value of -0.1123 mGal m^{-1}. Although it may be tempting to attribute these
765 differences solely to local density variations, interpreting the slope requires caution. It is
766 difficult to determine whether these deviations are primarily related to topographic effects,
767 such as those linked to the degree of isostatic compensation, or to actual density
768 heterogeneities. The latter may include denser volcanic or mafic bodies and less dense

sedimentary basins, both capable of producing localized gravity anomalies that affect the regression slope independently of the large-scale isostatic signal.

The slope map (Fig. 7) illustrates the spatial variability of the regression gradient between Bouguer anomaly and filtered topography, providing an overview of the degree and nature of isostatic compensation across Antarctica. The theoretical slope value (−0.1123 mGal m^{-1}) predominates across the continent, where light-purple tones are most extensive. More negative slopes than predicted (down to −0.2246 mGal m^{-1}; yellow tones) occur over Wilkes Land, including the Wilkes Subglacial Basin and the George V Coast, and extend into parts of Marie Byrd Land, the Ferrigno Rift, and the Ross Sea, as well as a few isolated areas in East Antarctica. Positive slope values (up to +0.1123 mGal m^{-1}; pink tones) are observed in the Aurora Subglacial Basin (ASB), Knox Subglacial Basin (KSB), West Ragnhild Trough (WRT), parts of the Adventure Subglacial Trench (AST), the Polar Gap region, and the Siple Coast–Ross Ice Shelf sector. Locally higher positive slopes (> +0.1123 mGal m^{-1}) occur near the continental-shelf break of the Weddell Sea sector, coinciding with regions of steep bathymetric gradient and limited direct bathymetric control reported in the IBCSO and RID compilations (Arndt et al., 2013; Dorschel et al., 2022). These regional variations may be influenced by contrasting subsurface structures, such as fault-bounded depressions and subglacial basins with sedimentary infill in the Wilkes Subglacial Basin (Ferraccioli et al., 2009), consistent with the occurrence of more negative slopes, and variable crustal thickness or mafic intrusions in parts of East Antarctica (Ferraccioli et al., 2011), possibly contributing to locally positive slopes.

The coincidence between positive slopes and positive correlations (Fig. 4) may therefore indicate regions that depart from the expected Airy-type compensation**,** where the gravity field increases with elevation. Such behavior may arise from locally dense or rigid crustal domains, where the Bouguer anomaly increases with elevation rather than decreasing as predicted by the

Airy model. Conversely, strongly negative slopes may indicate areas where topography is more effectively compensated or where low-density crustal sections contribute to the gravity field**.** The combined distribution of slope and intercept values reveals a complementary pattern across the continent. Regions where the slope reaches its most negative values (~−0.2246 mGal m^{-1}) correspond to areas where the intercept remains close to zero, indicating that the Bouguer anomaly varies proportionally with topography with little systematic regression offset**,** and broadly consistent with a gravity–topography relationship close to that predicted by Airy-type compensation. In contrast, sectors where the intercept becomes strongly negative coincide with positive slope values (~+0.1123 mGal m^{-1}), marking domains where the Bouguer anomaly increases with elevation. Such behavior is consistent with rigid or dense crustal regions in which compensation is limited, and the gravity field reflects the contribution of high-density material or reduced crustal thickness. Together, these patterns indicate that the gravity field reflects the superposition of two components: a topography-dependent signal associated with crustal compensation, expressed by the regression slope, and a regional gravity offset related to deeper lithospheric density variations, captured by the intercept.

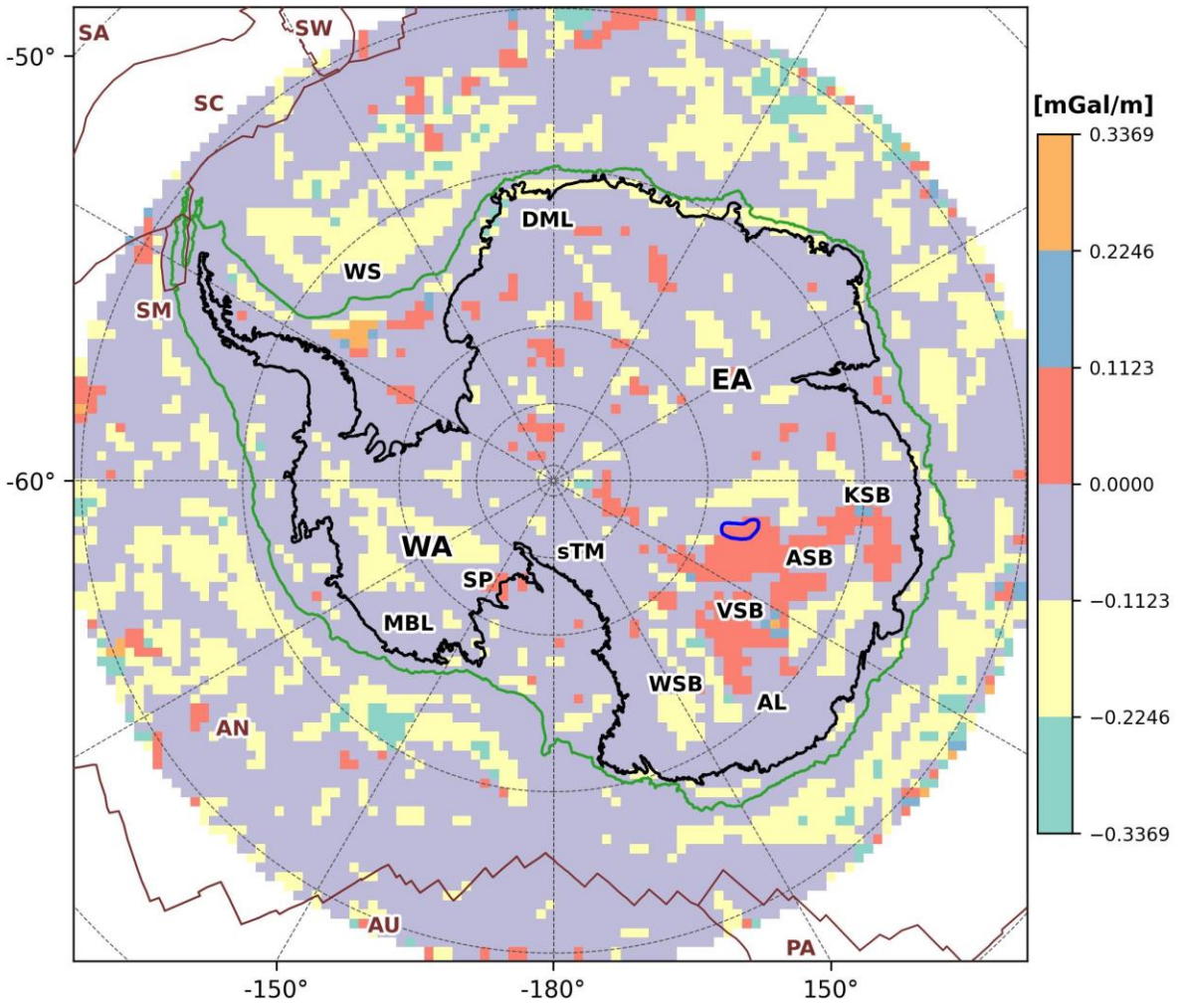

Figure 7. Slope of the regression between Bouguer anomaly and filtered topography, illustrating regional deviations from the theoretical Airy value (−0.1123 mGal m^{-1}). Abbreviations of geological features are the same as in Fig. 2.

4.6 Summary of regression parameters

The main regression parameters discussed in the previous sections are summarized below (Table 1). This synthesis does not introduce new interpretations but reorganizes, in a comparative framework, the observed conditions and geological meanings already described for each variable. The table highlights how individual parameters—correlation, coefficient of determination (R^2), intercept, slope, and residuals—reflect different aspects of the gravity–topography relationship, crustal density contrasts, and the mechanisms of isostatic compensation across Antarctica.

823 **Table 1 – Single parameter interpretation**

Parameter(s)	Observed conditions / Typical range	Individual interpretation	Geophysical / Geological implications
Residual map (Fig. 2)	Local highs ≈ +30 mGal (v, shelf edge); lows ≈ −30 mGal (Knox Subglacial Basin, Dronning Maud Land)	Point-wise deviation from the regression-predicted gravity	Marks local density variations and topographic edge effects; useful for identifying structural boundaries.
Low RMSE (Fig. 3)	RMSE < ~6 mGal; (e.g., Antarctic Peninsula, Marie Byrd Land, large portions of the continental shelf)	Small dispersion of Bouguer anomaly values around the regression-predicted gravity	Reflects a coherent large-scale gravity–topography coupling, suggesting that the gravity field is largely controlled by the mass distribution associated with the topographic load and its compensating root.
High RMSE (Fig. 3)	RMSE > ~14mGal;	Large dispersion of Bouguer anomaly values around the regression-predicted gravity	Suggests the presence of additional mass contributions not captured by the regression model, such as lateral density heterogeneities, sedimentary basins, crustal thickness variations, or strong topographic gradients.
Regression residual (Fig. 19, Supporting informartion)	WA and Continental shelf ≈ 0 (numerical precision); EA: minor variability ($\sim 10^{-13}$).	Window-averaged misfit is minimal at continental scale.	Highlights the large-scale WA–EA contrast in gravity–topography behavior and delineates the continental shelf edge.
Positive correlation (Fig 4)	$r > 0$ (localized regions in East Antarctica, Shetland sector, and near the Weddell shelf break)	Bouguer anomaly increases with elevation, departing from the inverse relationship expected under local	May reflect undercompensation, lithospheric rigidity and regional compensation, or lateral density

		Airy-type compensation.	heterogeneities within the crust or upper mantle.
Negative correlation (Fig 4)	$r < 0$ (dominant across most of Antarctica)	Elevated topography corresponds to negative Bouguer anomalies.	Consistent with gravity variations dominated by crustal thickness variations, broadly compatible with Airy-type isostatic compensation.
Near-zero correlation (Fig 4)	$r \approx 0$ (scattered, e.g., parts of Adélie Land and EA interior)	Weak or absent linear relationship.	Suggests heterogeneous or compositionally variable crust or non-linear responses.
Low R^2 (Fig. 4)	< 0.4 (Wilkes Land, Coats Land, parts of Weddell sector)	Weak relationship between topography and gravity anomaly.	Suggests alternative compensation mechanisms (e.g., Pratt or flexural isostasy) or complex crustal/lithospheric heterogeneities not captured by a simple Airy model.
High R^2 (Fig. 4)	> 0.8 Antarctic Peninsula, Marie Byrd Land, southern Transantarctic Mountains)	Topography explains most of the gravity variation.	Suggests locally effective Airy-type compensation, although thermally driven anomalies may also yield high fit quality.
Positive intercept (Fig. 6)	$b>0$ (e.g., Weddell Sea margin, Marie Byrd Land)	Systematic positive gravity offset.	May reflect shallow Moho or dense lithospheric material.
Negative intercept (Fig. 6)	$b < 0$ (predominant in EA interior; also Ross Sea)	Systematic negative gravity shift.	Indicates a long-wavelength regional gravity offset associated with laterally extensive density contrasts, decoupled from local topographic compensation; consistent with the regional Moho contrast between WA and EA.

Slope ≈ −0.1123 mGal m^{-1} (Fig. 7)	Close to theoretical $-2\pi G\rho c$ (ρc = 2.67 g cm^{-3})	Regression slope matches the Airy theoretical value.	Indicates near-ideal Airy isostatic compensation.
More negative slope (Fig. 7)	≈ −0.2246 mGal m^{-1} (e.g., Wilkes Land, Ross Sea)	Bouguer anomaly decreases with elevation more strongly than predicted by the Airy model	Suggests overcompensated or low-density crustal domains where gravity varies more strongly with elevation than predicted by the Airy model.
Positive slope (Fig. 7)	≈ +0.1123 mGal m^{-1} (e.g Aurora Subglacial Basin, Knox Subglacial Basin; locally near Weddell shelf break)	Bouguer anomaly increases with elevation.	Indicates limited compensation and/or dense or rigid crustal domains.

The combined relationships among regression parameters are summarized below (Table 2). It organizes how specific parameter pairings refine the interpretation of the gravity–topography relationship, distinguishing regions that approximate near-isostatic behavior from those influenced by lateral density contrasts, thermal structure, or compositional heterogeneity within the crust and lithosphere.

Table 2: Combined parameter interpretation

Parameter combination	**Observed conditions / Typical range**	**Joint interpretation**	**Geophysical / Geological implications**
Negative correlation (>0.8) and negative residuals (Fig. 4 and Fig. 2)	Dronning Maud Land	Strong inverse relation between gravity and topography combined with gravity values lower than predicted by the regression.	Indicates local mass deficit relative to the regression trend, consistent with nearly complete or slightly overcompensated isostatic equilibrium
Negative correlation (>0.8) and positive residuals (Fig. 4 and Fig. 2)	Transantarctic Mountains	Strong inverse relation between gravity and topography but with gravity higher than	Suggests localized excess mass at depth beneath elevated topography, consistent crustal

		predicted by the regression.	density variations or mantle upward providing non-Airy support for the range.
Positive correlation and negative residuals (Fig. 4 and Fig. 2)	Lake Vostok, Knox Subglacial Basin, Adventure Subglacial Basin, Vincennes Subglacial Basin	Positive correlation coincides with negative residuals.	Suggests regional compensation mechanism and local mass deficit, consistent with low-density material beneath subglacial depressions
Positive correlation and positive residuals(Fig. 4 and Fig. 2)	West of the northwestern boundary of the South Shetland Microplate (residual > 20 mGal)	Both gravity and topography increase together, and the gravity field is stronger than predicted by the regression.	Suggests structural complexities and lateral density contrasts near the transition between continental and oceanic crust.
Positive correlation and + low RMSE (Fig. 4 and Fig. 3)	r > 0 and RMSE < ~6 mGal (e.g. Localized regions of East Antarctica)	The Bouguer anomaly increases with elevation while remaining closely aligned with the linear regression relationship.	May reflect lithospheric rigidity and flexural support of topography.
Positive correlation + high RMSE (Fig. 4 and Fig. 3)	r > 0 and RMSE > ~14 mGal (e.g. Lake Vostok, Adélie Land)	Bouguer anomaly increases with elevation but displays large dispersion around the regression relationship.	Suggests localized density heterogeneities, sedimentary basins, or complex crustal structure.
Negative intercept and positive correlation (Fig. 6 and Fig. 4)	East Antarctica interior (e.g., Wilkes Land, Coats Land)	Negative intercepts coincide with positive correlation values.	May indicate dense lower-crustal domains or lithospheric density contrasts influencing the gravity field independently of local topography.
Negative intercept and negative correlation (Fig. 6 and Fig. 4)	Ross Sea Basins	Negative intercepts associated with negative correlation.	Consistent with deep-seated, laterally extensive density contrasts, potentially related to rifting and crustal thinning.

Negative intercept and low R^2 (Fig. 6 and Fig. 5)	Wilkes Land, Coats Land, Weddell Sea	Pronounced intercept offset with poor regression fit.	Indicates variable crustal density or non-linear response where local geological complexity reduces the representativeness a simple gravity–topography regression model.
Positive slope and positive correlation (Fig. 7 and Fig. 4)	Knox Subglacial Basin, Aurora Subglacial Basin, Weddell margin	Both gravity and topography increase together.	May reflect departure from local Airy-type compensation, possibly associated with localized density contrasts or thermal effects in the crust or upper mantle.
High R^2, strong negative correlation and residuals ≈ 0 (Fig. 5, Fig. 4 and Fig. 2)	Antarctic Peninsula, southern Transantarctic Mountains	Strong linear fit and near-zero residuals.	Gravity–topography relation consistent with large-scale Airy-type or thermally influenced density structure, reflecting a stable long-wavelength relation between gravity and topography.
High R^2 + low RMSE (Fig. 5 and Fig. 3)	R^2 > ~80% and RMSE < ~6 mGal	Strong linear relationship between Bouguer anomaly and filtered topography with small dispersion around the regression.	Consistent with large-scale compensation mechanisms such as Airy-type crustal roots or lithospheric-scale density variations
Low to moderate R^2, positive correlation and/or large residuals (Fig. 5 and Fig. 2)	Lake Vostok, Knox Subglacial Basin, Adélie Land	Weak statistical fit and anomalous gravity–topography relation.	Indicates local departures from Airy-type compensation, reflecting lateral density contrasts, incomplete isostatic adjustment, or thermally perturbed

lithospheric domains.

4.7 Comparison with probabilistic basin likelihood models

The regression-based results presented here show convergence with the probabilistic mapping of subglacial sedimentary basins by Li et al. (2022) (their fig. 2; Fig. 8 in this study), whose decision tree model integrates multiple geophysical and geological inputs such as gravity, magnetic anomalies, crustal thickness, and seismic data to estimate basin likelihood. The present analysis relies solely on the statistical relationship between Bouguer anomaly and topography, providing an independent assessment of subsurface density contrasts.

Despite these methodological differences, regions identified as likely basins by Li et al. (2022), including the Aurora Subglacial Basin (ASB), Knox Subglacial Basin (KSB), and Vincennes Subglacial Basin (VSB), coincide with areas where the regression results show a clear signal. In these regions, the regression analysis is characterized by positive Bouguer–topography correlation, negative residuals, low coefficients of determination ($R^2 < 30\%$), negative intercept values, low RMSE values (< 6 mGal), and slopes close to ~0.1123. The correspondence between basin candidates identified by the regression analysis and the probabilistic basin likelihood model of Li et al. (2022) is summarized in Table 3.

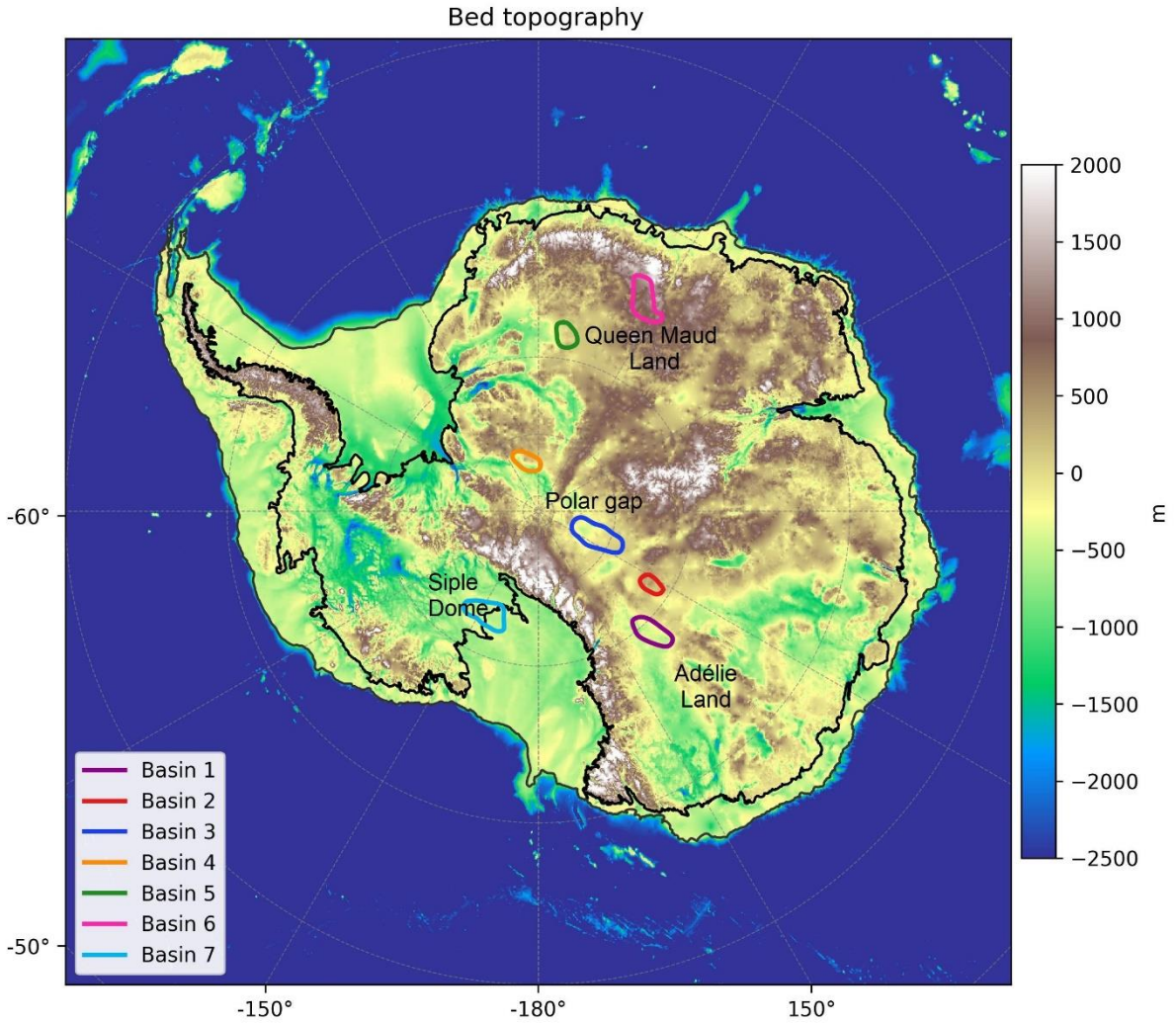

Figure 8: Candidate sedimentary basins identified from the regression analysis between Bouguer anomaly and filtered equivalent topography. The background image shows bed elevation from Morlighem et al. (2020). Basins 1–5 coincide with regions classified as moderate- to high-likelihood sedimentary basins in the probabilistic model of Li et al. (2022), whereas Basins 6 and 7 represent additional candidates highlighted by the present analysis.

In addition to these previously recognized regions, both approaches also highlight several new areas with high basin likelihood. The regression maps delineate additional candidate zones (Fig. 8) that were also classified as high-likelihood (>0.6) basins by Li et al. (2022), including Adélie Land (Basin 1, Fig. 8), portions of the Polar Gap (Basins 2–4, Fig. 8), and part of Queen Maud Land (Basin 5, Fig. 8). Finally, two additional basin candidates emerge from our analysis. One of these areas (Basin 6, Fig. 8) is classified as low likelihood (<0.3) in the

probabilistic model, whereas the other, located at Siple Dome (Basin 7, Fig. 8) corresponds to an intermediate basin likelihood (~0.5).

Table 3: Regression basin candidates and probabilistic basin likelihood

Basin / Region	Status in this study	Corresponding region in Li et al. (2022)	Basin likelihood in Li et al. (2022)
Aurora Subglacial Basin (ASB); Knox Subglacial Basin (KSB); Vincennes Subglacial Basin (VSB);	Previously recognized basin highlighted by regression maps	Aurora Subglacial Basin (ASB); Knox Subglacial Basin (KSB); Vincennes Subglacial Basin (VSB);	High (>0.6)
Basin 1 – Adélie Land	Candidate basin identified by regression analysis	High-likelihood basin region	
Basins 2–4 – Polar Gap	Candidate basin identified by regression analysis	High-likelihood basin region	High (>0.6)
Basin 5 – Queen Maud Land	Candidate basin identified by regression analysis	High-likelihood basin region	High (>0.6)
Basin 6 – Siple Coast	Candidate basin identified by regression analysis	Intermediate-likelihood basin region	Intermediate (~0.5)
Basin 7 – Queen Maud Land	Candidate basin identified by regression analysis	Low-likelihood basin region	Low (<0.3)

Note that the major basins used here as reference parameters to identify the criteria applied to propose new sedimentary basins (i.e., the Aurora (ASB), Knox (KSB), and Vincennes (VSB) Subglacial Basins) may represent a different geological and tectonic context compared to other previously identified basins that are not captured by the regression model. ASB, KSB, and VSB correspond to major sedimentary basins of Wilkes Land whose geometry is structurally controlled by regional faults and rift-related tectonic features (Aitken et al., 2014). These basins are interpreted as preserved sedimentary basins forming large subglacial depressions within

East Antarctica (Aitken et al., 2023). In contrast, the Wilkes Subglacial Basin, an example of a major basin not captured by the model, represents a structurally more complex system composed of distinct northern and southern subbasins with different sediment distributions and geological histories (Frederick et al., 2016). It has been interpreted as a possible retro-arc basin associated with the Ross Orogen and lies across a major tectonic boundary marked by the Mertz Shear Zone (Aitken et al., 2014). Accordingly, it is tentative to suggest that the basins proposed here, especially the newly identified ones (i.e., Basin 6 and Basin 7), may share geological characteristics with the Aurora, Knox, and Vincennes subglacial basins. However, more detailed geophysical investigations would be required to confirm whether these regions indeed correspond to sedimentary basins with comparable tectonic and geological configurations.

5. Conclusion

The gravity–topography regression analysis presented here provides a continent-scale assessment of the relationship between Bouguer anomaly and equivalent topography across Antarctica using satellite gravity data. The use of equivalent topography enables a consistent treatment of continental, marine, and ice-covered regions within a unified regression framework. The spatial distribution of the regression parameters reveals contrasting gravity–topography relationships associated with distinct lithospheric domains and compensation regimes across Antarctica. Regions such as the Antarctic Peninsula, Marie Byrd Land, and the southern Transantarctic Mountains are characterized by strong negative correlation, high R^2 values, and low residuals, indicating coherent long-wavelength coupling between gravity and topography. Although this behavior is compatible with Airy-type compensation within the adopted framework, comparison with seismic observations suggests that thermal anomalies and density variations within the lithospheric mantle may generate a similar gravimetric response. In contrast, large sectors of East Antarctica exhibit positive Bouguer–topography

correlation, low to moderate R^2 values, negative intercepts, and localized residual anomalies. Together with independent seismic evidence for thick and cold lithosphere, these patterns indicate that the gravity field is controlled not only by local crustal compensation, but also by lithospheric rigidity, regional compensation, and lateral density heterogeneities . The combined distribution of correlation, R^2, slope, intercept, residuals, and RMSE further differentiates regions characterized by coherent gravity–topography coupling from areas dominated by localized density anomalies and complex lithospheric structure. Several regions identified by the regression analysis coincide with previously proposed subglacial sedimentary basins, including the Aurora, Knox, and Vincennes basins, while additional candidate regions are also highlighted by the analysis. In these areas, the regression parameters consistently combine positive Bouguer–topography correlation, negative residuals, low R^2 values, negative intercepts, low RMSE values, and slopes close to +0.1123 mGal m^{-1}. Overall, the results indicate that the large-scale gravity field of Antarctica reflects the coexistence of distinct compensation mechanisms, lithospheric rigidity contrasts, and crustal density heterogeneities. These findings provide new constraints on the lithospheric and tectonic framework of the Antarctic continent.

Acknowledgements

This work was funded by National Science Foundation 2114502. We thank Tomasso Pivetta for discussion contributions.

Author contributions Statement: Renata Regina Constantino conceived the study, processed the data, performed the regression analysis and interpretation, and wrote the manuscript. Kirsty Tinto contributed to the development and discussion of the study throughout all stages of the work, including interpretation of the results and manuscript preparation. Leonardo Uieda contributed to the computation of the Bouguer anomaly,

discussion of the results, and manuscript preparation. Carla Braitenberg contributed to the interpretation and discussion of the regression analysis and manuscript preparation. All authors contributed to the revision of the manuscript

Data Availability Statement: The GOCO06S satellite gravity model used in this study is publicly available through the International Centre for Global Earth Models (ICGEM) at ICGEM. Gravity disturbance grids were obtained using the ICGEM calculation service (product "gravity_disturbance_sa"). Bed elevation and ice-thickness data were obtained from BedMachine Antarctica v3 (Morlighem et al., 2020), available at NSIDC BedMachine Antarctica v3. All derived regression products, figures, data, and software code generated in this study are available from the corresponding author upon publication through a public repository.

6. References

Aitken, A. R. A., Young, D. A., Ferraccioli, F., Betts, P. G., Greenbaum, J. S., Richter, T. G., ... & Siegert, M. J. (2014). The subglacial geology of Wilkes land, East Antarctica. *Geophysical Research Letters*, *41*(7), 2390-2400.

An, M., Wiens, D. A., Zhao, Y., Feng, M., Nyblade, A. A., Kanao, M., ... & Lévêque, J. J. (2015). S-velocity model and inferred Moho topography beneath the Antarctic Plate from Rayleigh waves. *Journal of Geophysical Research: Solid Earth*, *120*(1), 359-383. https://doi.org/10.1002/2014JB011332

Amblas, D. (2018): Antarctic continental shelf break (shapefile) [dataset]. Scott Polar Research Institute, University of Cambridge, PANGAEA, https://doi.org/10.1594/PANGAEA.890863

Arndt, Jan Erik; Schenke, Hans Werner; Jakobsson, Martin; Nitsche, Frank-Oliver; Buys, Gwen; Goleby, Bruce; Rebesco, Michele; Bohoyo, Fernando; Hong, Jong Kuk; Black, Jenny; Greku, Rudolf Kh; Udintsev, Gleb B; Barrios, Felipe; Reynoso-Peralta, Walter; Taisei, Morishita; Wigley, Rochelle (2013): The International Bathymetric Chart of the Southern Ocean (IBCSO) Version 1.0 [dataset publication series]. PANGAEA, https://doi.org/10.1594/PANGAEA.805736

Baranov, A., & Morelli, A. (2013). The Moho depth map of the Antarctica region. *Tectonophysics*, *609*, 299-313. https://doi.org/10.1016/j.tecto.2012.12.023

Barthelmes, F. (2013). Definition of functionals of the geopotential and their calculation from spherical harmonic models.
http://publications. iass-potsdam. de/pubman/item/escidoc, *104132*(3), 0902-2.

Behrendt, J. C., & Popenoe, P. (1969). Basement Structure Contour Map of North Park–Middle Park Basin, Colorado. *AAPG Bulletin*, *53*(3), 678-682. https://doi.org/10.1306/5D25C6A7-16C1-11D7-8645000102C1865D

Bell, R. E. (1989). Structure of continental margins from gravity anomalies: The margins of the western Weddell Sea (Chapter 3). In *High-resolution marine and airborne gravity surveys: applications to rifted margins* (PhD Thesis, Columbia University).
https://doi.org/10.7916/5255-rw74

Berg, D., Barletta, V. R., Hassan, J., Lippert, E. Y. H., Colgan, W., Bevis, M., ... & Khan, S. A. (2024). Vertical land motion due to present-day ice loss from Greenland's and Canada's peripheral glaciers. *Geophysical Research Letters*, *51*(2), e2023GL104851. https://doi.org/10.1029/2023GL104851

Bird, P. (2003). An updated digital model of plate boundaries. *Geochemistry, Geophysics, Geosystems*, *4*(3). https://doi.org/10.1029/2001GC000252

Blakely, R. J. (1996). *Potential theory in gravity and magnetic applications*. Cambridge university press

Braitenberg, C. (2015). Exploration of tectonic structures with GOCE in Africa and across-continents. *International Journal of Applied Earth Observation and Geoinformation*, *35*, 88-95. https://doi.org/10.1016/j.jag.2014.01.013

Carter, S. P., Blankenship, D. D., Peters, M. E., Young, D. A., Holt, J. W., & Morse, D. L. (2007). Radar-based subglacial lake classification in Antarctica. *Geochemistry, Geophysics, Geosystems*, *8*(3). https://doi.org/10.1029/2006GC001408

Catalán, M., Galindo-Zaldivar, J., Davila, J. M., Martos, Y. M., Maldonado, A., Gambôa, L., & Schreider, A. A. (2013). Initial stages of oceanic spreading in the Bransfield Rift from magnetic and gravity data analysis. *Tectonophysics*, *585*, 102-112. https://doi.org/10.1016/j.tecto.2012.09.016

Chaput, J., Aster, R. C., Huerta, A., Sun, X., Lloyd, A., Wiens, D., ... & Wilson, T. (2014). The crustal thickness of West Antarctica. *Journal of Geophysical Research: Solid Earth*, *119*(1), 378-395. https://doi.org/10.1002/2013JB010642

Chen, J. L., Wilson, C. R., Blankenship, D. D., & Tapley, B. D. (2006). Antarctic mass rates from GRACE. *Geophysical research letters*, *33*(11). https://doi.org/10.1029/2006GL026369

Cochran, J. R. (1979). An analysis of isostasy in the world's oceans: 2. Midocean ridge crests. *Journal of Geophysical Research: Solid Earth*, *84*(B9), 4713-4729. https://doi.org/10.1029/JB084iB09p04713

Cochran, J. R., Tinto, K. J., & Bell, R. E. (2015). Abbot Ice Shelf, structure of the Amundsen Sea continental margin and the southern boundary of the Bellingshausen Plate seaward of West Antarctica. *Geochemistry, Geophysics, Geosystems*, *16*(5), 1421-1438. https://doi.org/10.1002/2014GC005570

Depoorter, M. A., Bamber, J. L., Griggs, J., Lenaerts, J. T. M., Ligtenberg, S. R. M., van den Broeke, M. R., & Moholdt, G. (2013). Antarctic grounding line. *PANGAEA*. https://doi.org/10.1594/PANGAEA.819150

Dorschel, B., Hehemann, L., Viquerat, S., Warnke, F., Dreutter, S., Tenberge, Y. S., ... & Arndt, J. E. (2022). The international bathymetric chart of the southern ocean version 2. *Scientific Data*, *9*(1), 275. https://doi.org/10.1038/s41597-022-01366-7

Ebbing, J., Haas, P., Ferraccioli, F., Pappa, F., Szwillus, W., & Bouman, J. (2018). Earth tectonics as seen by GOCE-Enhanced satellite gravity gradient imaging. *Scientific reports*, *8*(1), 16356. DOI:10.1038/s41598-018-34733-9

Ferraccioli, F., Armadillo, E., Jordan, T., Bozzo, E., & Corr, H. (2009). Aeromagnetic exploration over the East Antarctic Ice Sheet: a new view of the Wilkes Subglacial Basin. *Tectonophysics*, *478*(1-2), 62-77. https://doi.org/10.1016/j.tecto.2009.03.013

Ferraccioli, F., Finn, C. A., Jordan, T. A., Bell, R. E., Anderson, L. M., & Damaske, D. (2011). East Antarctic rifting triggers uplift of the Gamburtsev Mountains. *Nature*, *479*(7373), 388-392. doi:10.1038/nature10566

Fatiando a Terra Project, Castro, Y. M., Esteban, F. D., Li, L., Oliveira Jr, V. C., Pesce, A., Shea, N., Soler, S. R., Souza-Junior, G. F., Tankersley, M., Uieda, L., & Uppal, I. (2024). Harmonica v0.7.0: Forward modeling, inversion, and processing gravity and magnetic data (0.7.0). Zenodo. https://doi.org/10.5281/zenodo.13308312

Förste, C., Bruinsma, S., Rudenko, S., Abrikosov, O., Lemoine, J. M., Marty, J. C., ... & Biancale, R. (2016): EIGEN-6S4 A time-variable satellite-only gravity field model to d/o 300 based on LAGEOS, GRACE and GOCE data from the collaboration of GFZ Potsdam and GRGS Toulouse. V. 2.0. GFZ Data Services. https://doi.org/10.5880/icgem.2016.008

Gapais, D., Pelletier, A., Ménot, R. P., & Peucat, J. J. (2008). Paleoproterozoic tectonics in the Terre Adélie Craton (East Antarctica). *Precambrian Research*, *162*(3-4), 531-539. https://doi.org/10.1016/j.precamres.2007.10.011

Golynsky, A. V., Ferraccioli, F., Hong, J. K., Golynsky, D. A., Von Frese, R. R. B., Young, D. A., ... & Roberts, J. L. (2018). New magnetic anomaly map of the Antarctic. *Geophysical Research Letters*, *45*(13), 6437-6449. https://doi.org/10.1029/2018GL078153

Grikurov, G., Leitchenkov, G., Kamenev, E. N., Mikhalsky, E., Golynsky, A., Masolov, V. N., & Laiba, A. A. (2003). Antarctic tectonic and minerogenic provinces. *Arctic and Antarctic, Russian Academy of Sciences*, *2*, 26-47.

Hansen, S. E., Kenyon, L. M., Graw, J. H., Park, Y., & Nyblade, A. A. (2016). Crustal structure beneath the Northern Transantarctic Mountains and Wilkes Subglacial Basin: implications for

tectonic origins. *Journal of Geophysical Research: Solid Earth*, *121*(2), 812-825. https://doi.org/10.1002/2015JB012325

Harley, S. L. (2009). The geology of Antarctica. *GEOLOGY-Volume IV*, 405.

Hinze, W. J., Von Frese, R., & Saad, A. H. (2013). *Gravity and magnetic exploration: Principles, practices, and applications*. Cambridge university press.

Hirt, C., Kuhn, M., Featherstone, W. E., & Göttl, F. (2012). Topographic/isostatic evaluation of new-generation GOCE gravity field models. *Journal of Geophysical Research: Solid Earth*, *117*(B5). https://doi.org/10.1029/2011JB008878

Ince, E. S., Barthelmes, F., Reißland, S., Elger, K., Förste, C., Flechtner, F., & Schuh, H. (2019). ICGEM–15 years of successful collection and distribution of global gravitational models, associated services, and future plans. *Earth system science data*, *11*(2), 647-674. http://doi.org/10.5194/essd-11-647-2019.

Ji, F., Wu, L., & Zhang, Q. (2022). Gravity-derived Antarctic crustal thickness based on the Gauss-FFT method. *Geochemistry, Geophysics, Geosystems*, *23*(8), e2022GC010555. https://doi.org/10.1029/2022GC010555

Karner, G. D., Studinger, M., & Bell, R. E. (2005). Gravity anomalies of sedimentary basins and their mechanical implications: Application to the Ross Sea basins, West Antarctica. *Earth and Planetary Science Letters*, *235*(3-4), 577-596. https://doi.org/10.1016/j.epsl.2005.04.016

Kim, H. R., Golynsky, A. V., Golynsky, D. A., Yu, H., Von Frese, R. R. B., & Hong, J. K. (2022). New magnetic anomaly constraints on the Antarctic crust. *Journal of Geophysical Research: Solid Earth*, *127*(3), e2021JB023329. https://doi.org/10.1029/2021JB023329

Kvas, A., Brockmann, J. M., Krauss, S., Schubert, T., Gruber, T., Meyer, U., ... & Pail, R. (2020). GOCO06s–a satellite-only global gravity field model. *Earth System Science Data Discussions*, *2020*, 1-31. https://doi.org/10.5194/essd-13-99-2021

Lawver, L. A., Keller, R. A., Fisk, M. R., & Strelin, J. A. (1995). Bransfield Strait, Antarctic Peninsula active extension behind a dead arc. In *Backarc basins: Tectonics and magmatism* (pp. 315-342). Boston, MA: Springer US.

Li, L., Aitken, A., Lindsay, M., & Kulessa, B. (2021). Subglacial sedimentary basins focus key vulnerabilities of the Antarctic ice-sheet. https://doi.org/10.21203/rs.3.rs-1117673/v1

Lloyd, A. J., Wiens, D. A., Zhu, H., Tromp, J., Nyblade, A. A., Aster, R. C., ... & O'Donnell, J. P. (2020). Seismic structure of the Antarctic upper mantle imaged with adjoint tomography. *Journal of Geophysical Research: Solid Earth*, *125*(3). https://doi.org/10.1029/2019JB017823

Llubes, M., Seoane, L., Bruinsma, S., & Rémy, F. (2018). Crustal thickness of Antarctica estimated using data from gravimetric satellites. *Solid Earth*, *9*(2), 457-467. https://doi.org/10.5194/se-9-457-2018

Maritati, A., Aitken, A. R. A., Young, D. A., Roberts, J. L., Blankenship, D. D., & Siegert, M. J. (2016). The tectonic development and erosion of the Knox subglacial sedimentary basin, East Antarctica. *Geophysical Research Letters*, *43*(20), 10-728. https://doi.org/10.1002/2016GL071063

Morelli, C. (1990). The regional meaning of the Bouguer gravity anomalies in the Mediterranean. *Journal of geodynamics*, *12*(2-4), 123-136. https://doi.org/10.1016/0264-3707(90)90002-C

Morlighem, M., Rignot, E., Binder, T., Blankenship, D., Drews, R., Eagles, G., ... & Young, D. A. (2020). Deep glacial troughs and stabilizing ridges unveiled beneath the margins of the Antarctic ice sheet. *Nature geoscience*, *13*(2), 132-137. https://doi.org/10.1038/s41562-019-0510-8

Naumenko-Dèzes, M. O., Rolland, Y., Lamarque, G., Duclaux, G., Gallet, S., Bascou, J., & Ménot, R. P. (2020). Petrochronology of the Terre Adélie Craton (East Antarctica) evidences a long-lasting Proterozoic (1.7–1.5 Ga) tectono-metamorphic evolution—Insights for the connections with the Gawler Craton and Laurentia. *Gondwana Research*, *81*, 21-57. https://doi.org/10.1016/j.gr.2019.11.010

Pappa, F., Ebbing, J., & Ferraccioli, F. (2019). Moho depths of Antarctica: Comparison of seismic, gravity, and isostatic results. *Geochemistry, Geophysics, Geosystems*, *20*(3), 1629-1645. https://doi.org/10.1029/2018GC008111

Pastorutti, A., & Braitenberg, C. (2019). A geothermal application for GOCE satellite gravity data: modelling the crustal heat production and lithospheric temperature field in Central Europe. *Geophysical Journal International*, *219*(2), 1008-1031. https://doi.org/10.1093/gji/ggz344

Pavlis, N. K., Holmes, S. A., Kenyon, S. C., & Factor, J. K. (2012). The development and evaluation of the Earth Gravitational Model 2008 (EGM2008). *Journal of geophysical research: solid earth*, *117*(B4). https://doi.org/10.1029/2011JB008916

Paxman, G. J., Jamieson, S. S., Ferraccioli, F., Jordan, T. A., Bentley, M. J., Ross, N., ... & Casal, T. G. (2019). Subglacial geology and geomorphology of the pensacola-pole basin, East Antarctica. *Geochemistry, Geophysics, Geosystems*, *20*(6), 2786-2807. https://doi.org/10.1029/2018GC008126

Peltier, W. R. (2004). Global glacial isostasy and the surface of the ice-age Earth: the ICE-5G (VM2) model and GRACE. *Annu. Rev. Earth Planet. Sci.*, *32*(1), 111-149. https://doi.org/10.1146/annurev.earth.32.082503.144359

Pivetta, T., & Braitenberg, C. (2020). Sensitivity of gravity and topography regressions to earth and planetary structures. *Tectonophysics*, *774*, 228299. https://doi.org/10.1016/j.tecto.2019.228299

Rummel, R., Horwath, M., Yi, W., Albertella, A., Bosch, W., & Haagmans, R. (2011). GOCE, satellite gravimetry and antarctic mass transports. *Surveys in geophysics*, *32*(4), 643-657. DOI 10.1007/s10712-011-9115-5

Scheinert, M., Ferraccioli, F., Schwabe, J., Bell, R., Studinger, M., Damaske, D., ... & Richter, T. D. (2016). New Antarctic gravity anomaly grid for enhanced geodetic and geophysical studies in Antarctica. *Geophysical Research Letters*, *43*(2), 600-610. https://doi.org/10.1002/2015GL067439

Shen, W., Wiens, D. A., Stern, T., Anandakrishnan, S., Aster, R. C., Dalziel, I., ... & Winberry, J. P. (2018). Seismic evidence for lithospheric foundering beneath the southern Transantarctic Mountains, Antarctica. *Geology*, *46*(1), 71-74. https://doi.org/10.1130/G39555.1

Simons, M., Hager, B. H., & Solomon, S. C. (1994). Global variations in the geoid/topography admittance of Venus. *Science*, *264*(5160), 798-803. DOI: 10.1126/science.264.5160.798

Smith, B., Fricker, H. A., Gardner, A. S., Medley, B., Nilsson, J., Paolo, F. S., ... & Zwally, H. J. (2020). Pervasive ice sheet mass loss reflects competing ocean and atmosphere processes. *Science*, *368*(6496), 1239-1242. DOI: 10.1126/science.aaz5845

Stern, T. A., & ten Brink, U. S. (1989). Flexural uplift of the Transantarctic Mountains. *Journal of Geophysical Research: Solid Earth*, *94*(B8), 10315-10330. https://doi.org/10.1029/JB094iB08p10315

Studinger, M., Bell, R. E., Buck, W. R., Karner, G. D., & Blankenship, D. D. (2004). Sub-ice geology inland of the Transantarctic Mountains in light of new aerogeophysical data. *Earth and Planetary Science Letters*, *220*(3-4), 391-408. https://doi.org/10.1016/S0012-821X(04)00066-4

Tankersley, M. D., Horgan, H. J., Siddoway, C. S., Caratori Tontini, F., & Tinto, K. J. (2022). Basement topography and sediment thickness beneath Antarctica's Ross Ice Shelf. *Geophysical Research Letters*, *49*(10), e2021GL097371. https://doi.org/10.1029/2021GL097371Digital Object Identifier (DOI)

Tapley, B. D., Bettadpur, S., Watkins, M., & Reigber, C. (2004). The gravity recovery and climate experiment: Mission overview and early results. *Geophysical research letters*, *31*(9). DOI:10.1029/2004GL019779

Telford, W. M., Geldart, L. P., & Sheriff, R. E. (1990). *Applied geophysics*. Cambridge university press.

Turcotte, D. L., & Schubert, G. (2002). *Geodynamics*. Cambridge university press.

Wannamaker, P., Hill, G., Stodt, J., Maris, V., Ogawa, Y., Selway, K., ... & Feucht, D. (2017). Uplift of the central transantarctic mountains. *Nature Communications*, *8*(1), 1588. DOI: 10.1038/s41467-017-01577-2

Watts, A. B. (2001). *Isostasy and Flexure of the Lithosphere*. Cambridge University Press.

Taylor, F. W., Bevis, M. G., Dalziel, I. W., Smalley Jr, R., Frohlich, C., Kendrick, E., ... & Gudipati, K. (2008). Kinematics and segmentation of the South Shetland Islands-Bransfield basin system, northern Antarctic Peninsula. *Geochemistry, Geophysics, Geosystems*, *9*(4). https://doi.org/10.1029/2007GC001873

van Wijk, J. W., Lawrence, J. F., & Driscoll, N. W. (2008). Formation of the Transantarctic Mountains related to extension of the West Antarctic Rift system. *Tectonophysics*, *458*(1-4), 117-126. https://doi.org/10.1016/j.tecto.2008.03.009

Supporting information

Section 1: Calculation of Bouguer disturbance from layered mass model

The gravity effect of eleven distinct mass layers was computed using a prism-based forward modeling approach, implemented with the Harmonica package (Fatiando a Terra Project, https://doi.org/10.5281/zenodo.3628741). The calculations consider all relevant mass contributions within the study area using standard density values of 2670 kg/m³ for crustal rocks (ρ_c), 1030 kg/m³ for seawater (ρ_c), and 917 kg/m³ for ice (ρ_i).

Bed topography, ice thickness, geoid and masks for grounded and floating ice were obtained from BedMachine Antarctica v3 (Morlighem et al., 2020), and all geometries were referenced to the WGS84 ellipsoid. The mass distribution was discretized into a set of layers defined relative to the ellipsoid in order to correctly account for both grounded and floating ice conditions.

These configurations are schematically illustrated in Fig. S1, and the corresponding equations are presented below. The maps representing each step of the calculations are shown in Figs. S2–S12.

Grounded ice

In regions where the ice is grounded, three layers were considered:

1. The ice column, extending from the ice surface to the ellipsoid or to the ice base, where the ice base is above the ellipsoid (ρ_i)
2. The crustal layer between bed topography located above the ellipsoid and the ellipsoid itself (ρ_c).
3. The ice column, extending from the ellipsoid to the bed below the ellipsoid (ρ_i - ρ_c)

Floating ice with surface above the ellipsoid

In regions of floating ice where the ice surface lies above the ellipsoid, five layers were defined:

4. Ice above the ellipsoid, from the ice surface to the ellipsoid, with density ρ_i.
5. Ice below the ellipsoid, from the ellipsoid to the ice base, with density contrast $(\rho_i - \rho_c)$.
6. From the ellipsoid to the geoid lying below the ellipsoid $(-\rho_c)$.
7. From the geoid above the ellipsoid and the ellipsoid itself (ρ_w).
8. The water column $(\rho_w - \rho_c)$.

Floating ice with surface below the ellipsoid

In regions where floating ice lies entirely below the ellipsoid, three layers were considered:

9. The layer between the ellipsoid and the ice surface $(-\rho_c)$.
10. The ice column $(\rho_i - \rho_c)$.
11. The water column between the ice base and the seafloor, with density contrast $(\rho_w - \rho_c)$.

Additional notes: All layer contributions were computed independently and summed to obtain the total gravitational effect of the modeled mass distribution, which was subsequently removed from the gravity disturbance field to derive the Bouguer disturbance. Lake Vostok was not considered in these calculations. There is no grounded ice witch the surface lies bellow the ellipsoid.

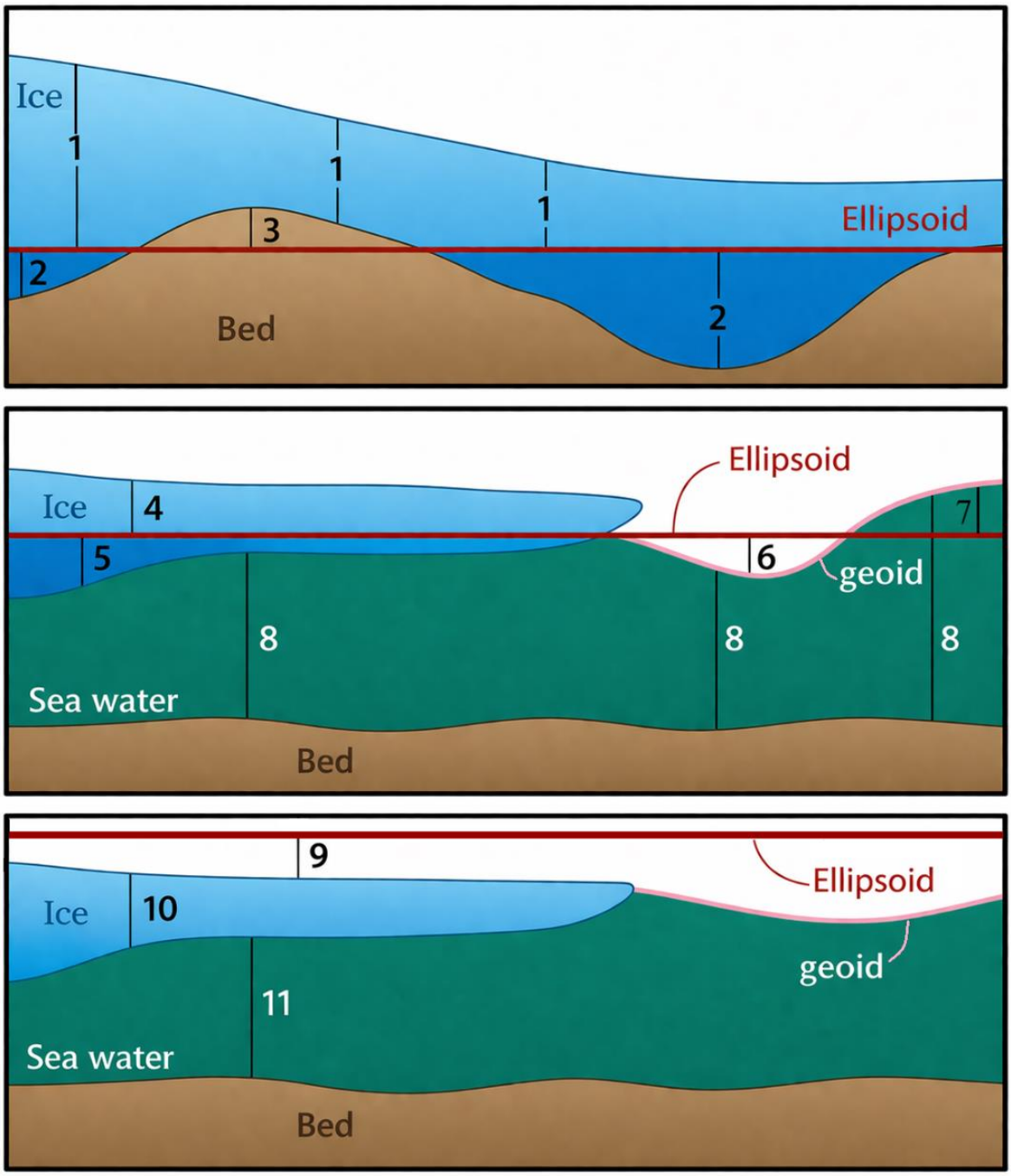

Figure S1. Schematic representation of the geometric configurations used to describe the vertical relationships between ice, sea water, bed topography, ellipsoid, and geoid. The three panels illustrate different scenarios depending on whether the ice and/or ocean are located above or below the reference surfaces. Numbered labels indicate the vertical components used in the formulation of the equations presented in the main text.

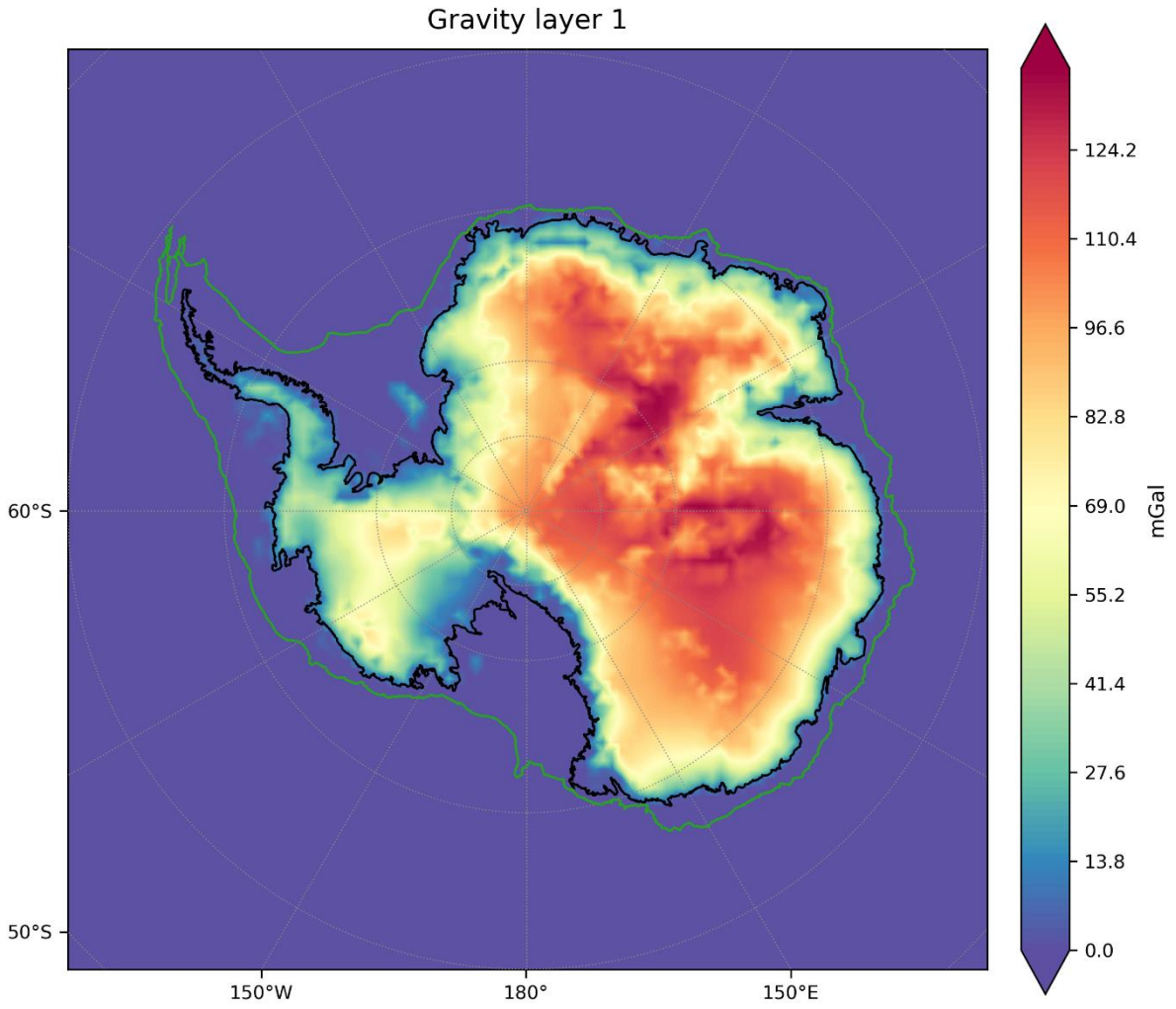

Figure S2: Gravity effect of the layer 1, defined as the ice column, extending from the ice surface to the ellipsoid or to the ice base, where the ice base is above the ellipsoid (ρ_i).

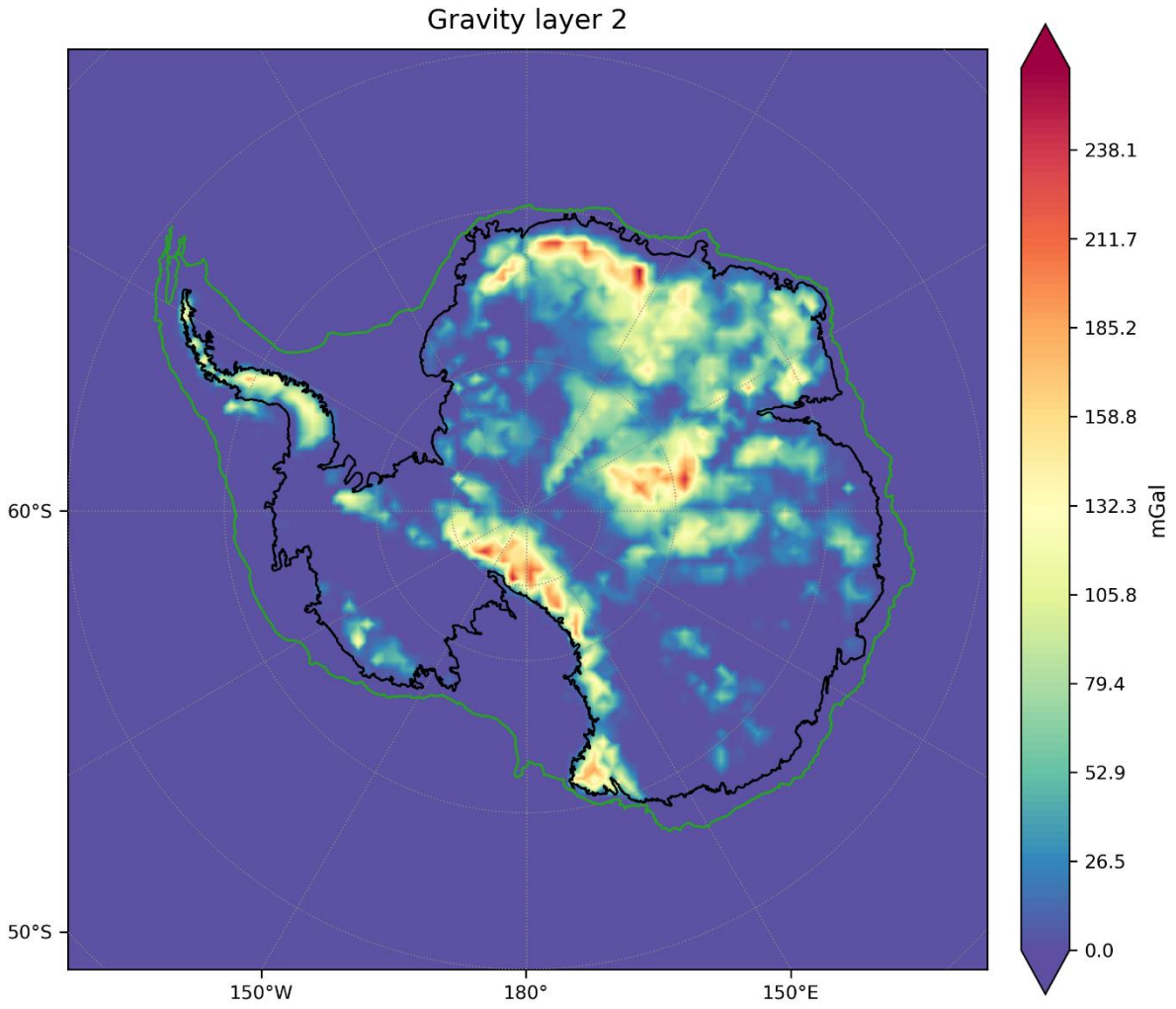

Figure S3: Gravity effect of the layer 2, defined as the ice column, extending from the ellipsoid to the bed below the ellipsoid (ρ_c - ρ_i).

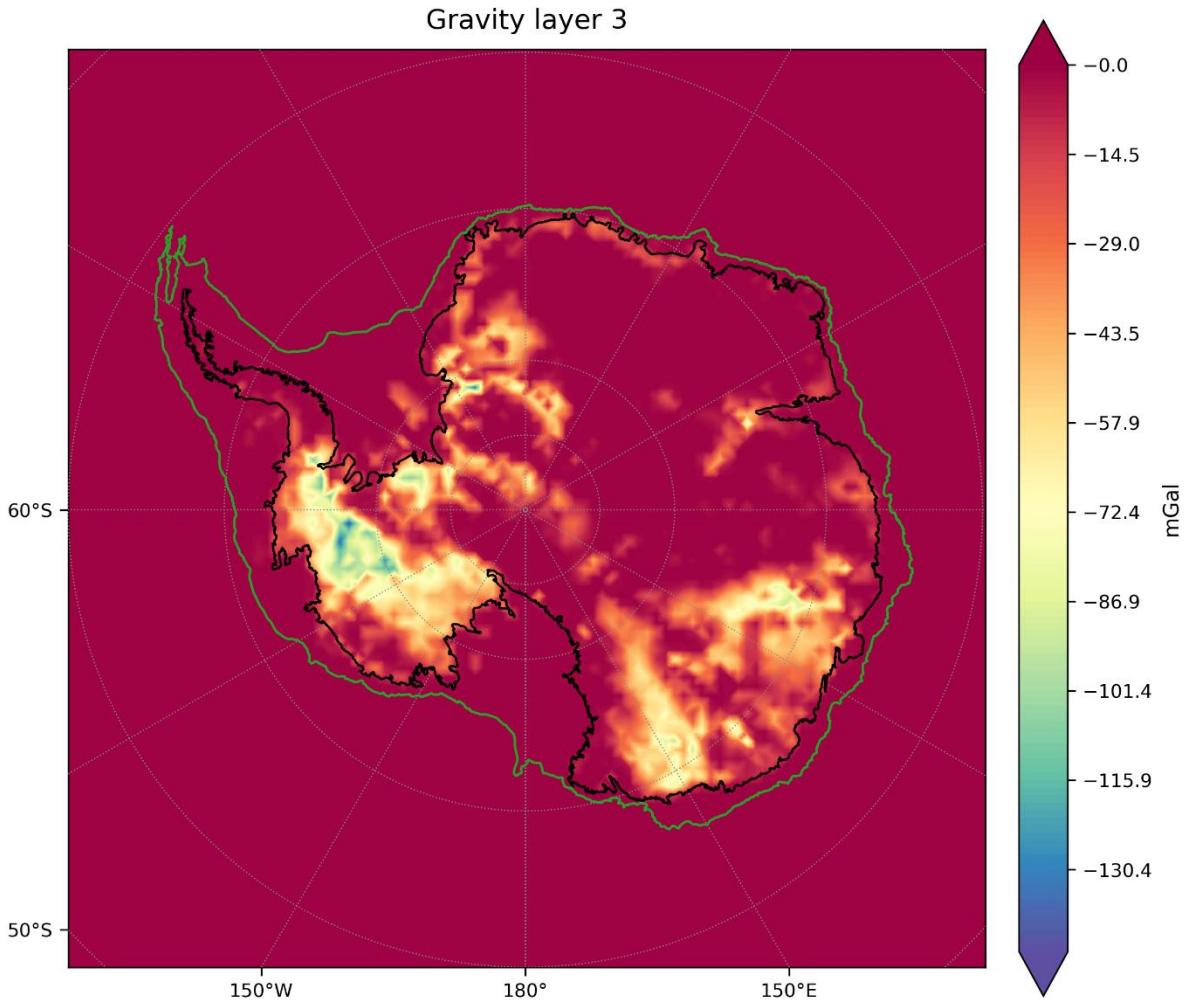

Figure S4: Gravity effect of the layer 3, defined as the crustal layer between bed topography located above the ellipsoid and the ellipsoid itself (ρ_c).

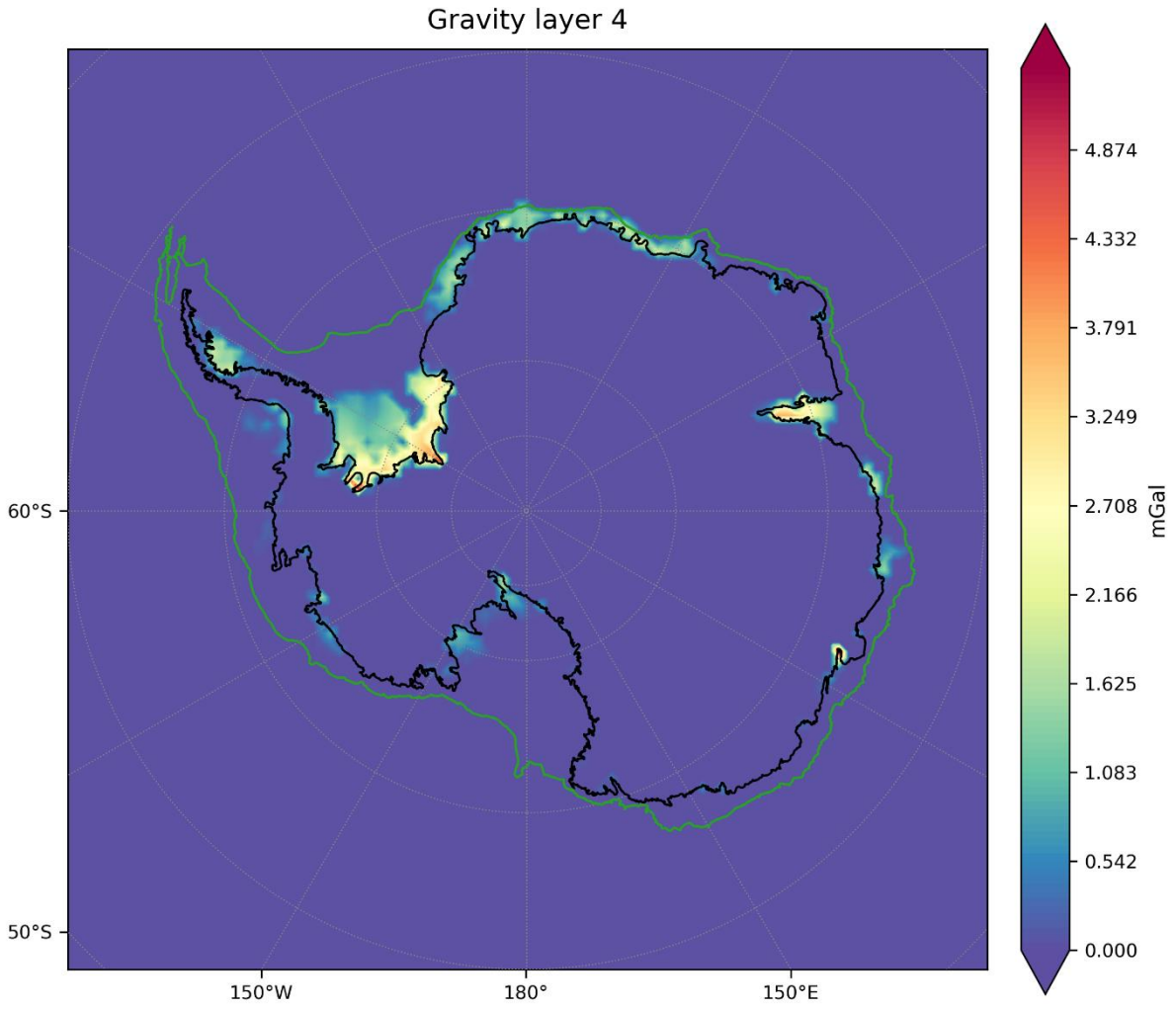

Figure S5: Gravity effect of the layer 4, defined as the ice above the ellipsoid, from the ice surface to the ellipsoid, with density ρ_i.

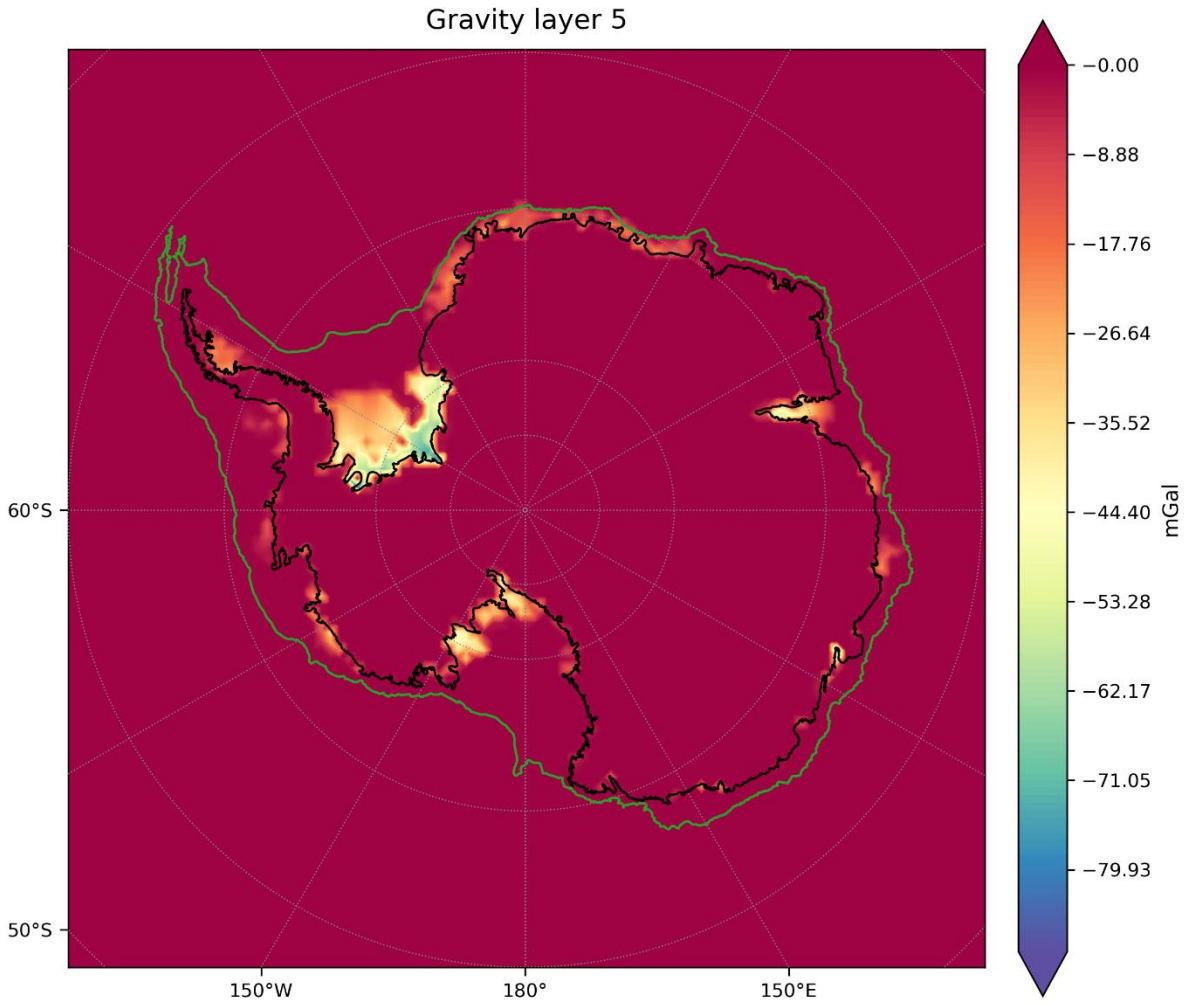

Figure S6: Gravity effect of the layer 5, defined as the ice below the ellipsoid, from the ellipsoid to the ice base, with density contrast ($\rho_i - \rho_c$)

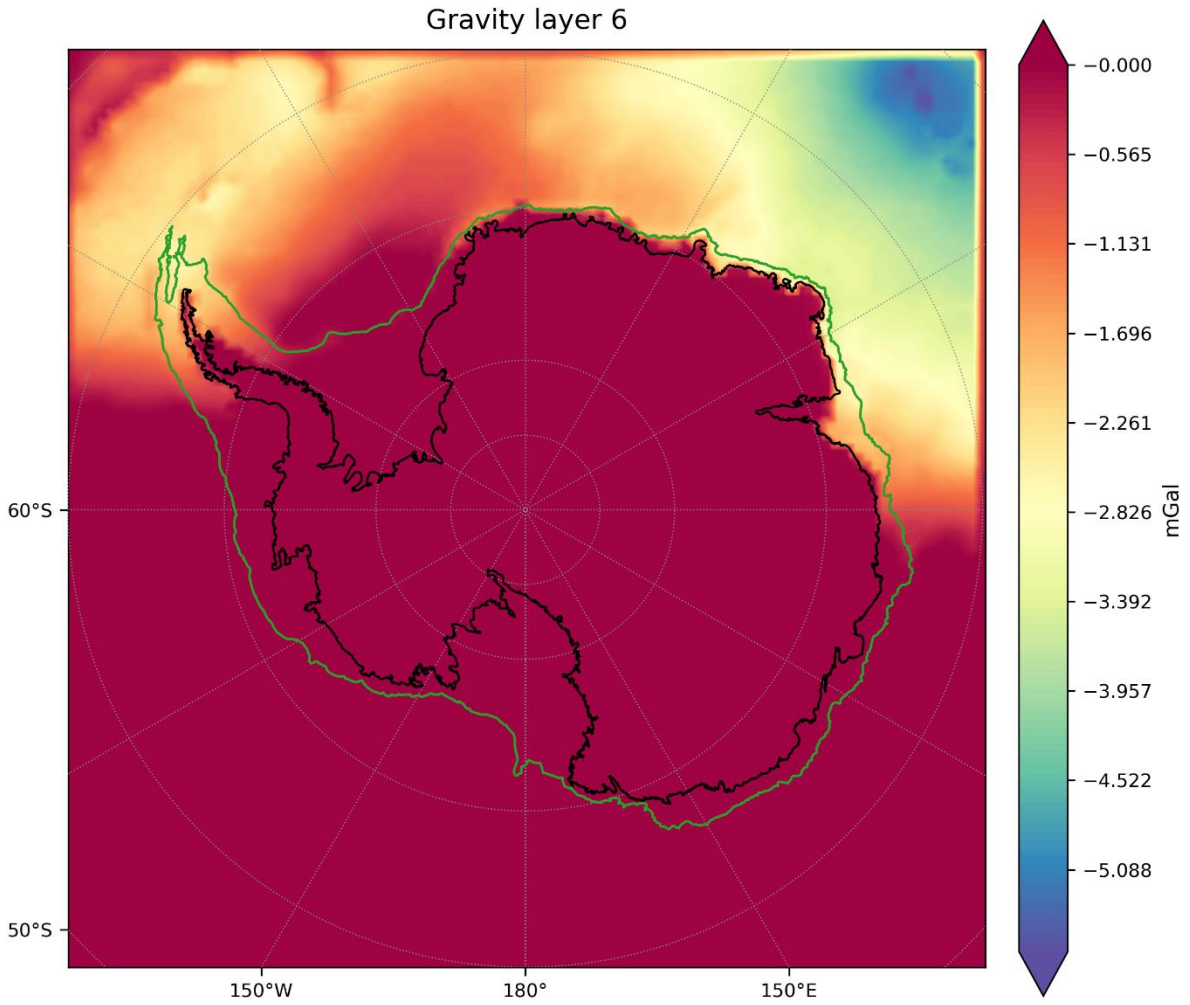

Figure S7: Gravity effect of the layer 6, defined from the ellipsoid to the geoid lying below the ellipsoid (−ρ_w).

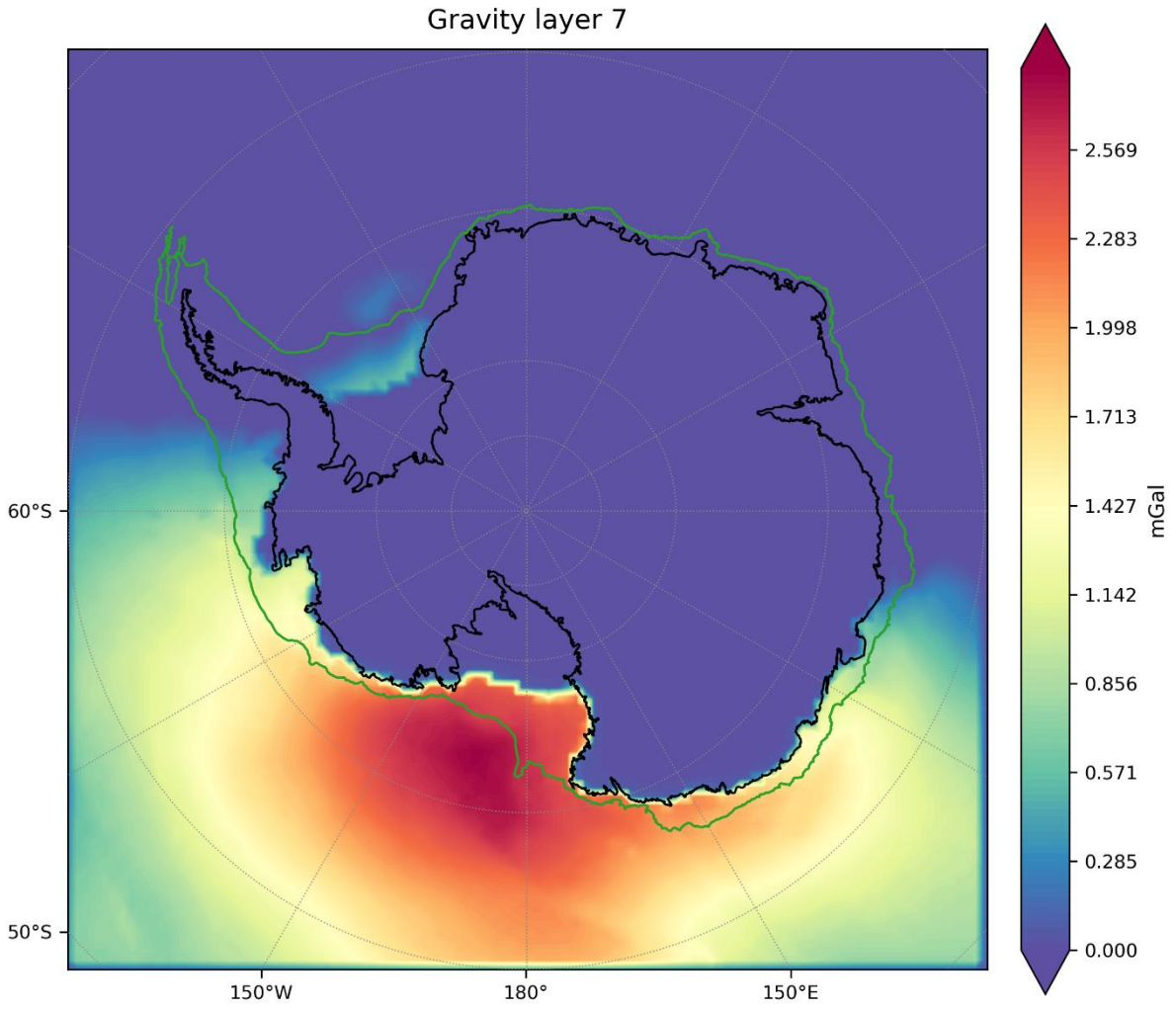

Figure S8: Gravity effect of the layer 7, defined from the geoid above the ellipsoid and the ellipsoid itself (ρ _w).

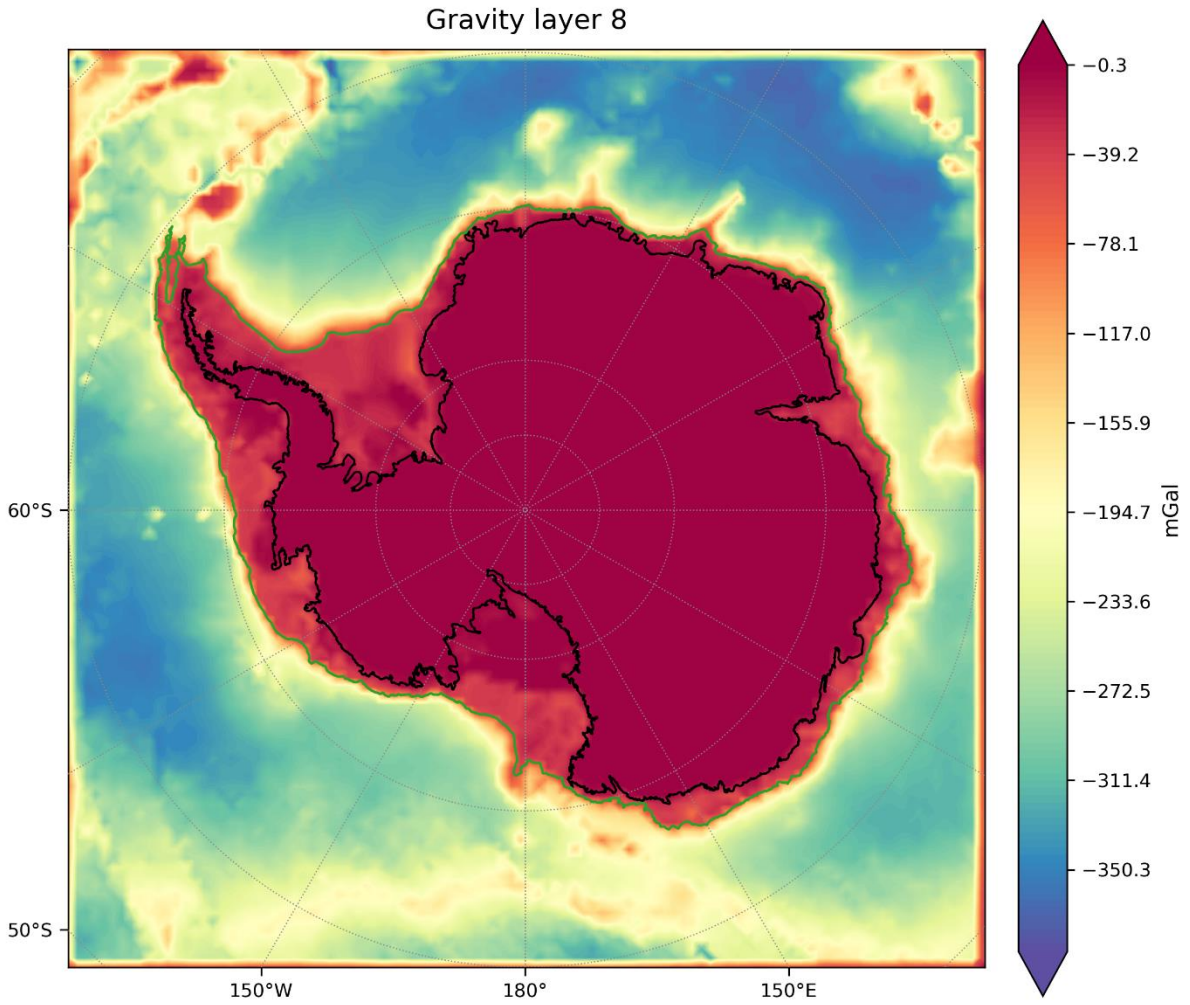

Figure S9: Gravity effect of the layer 8, defined as the water column (ρ_w − ρ_c).

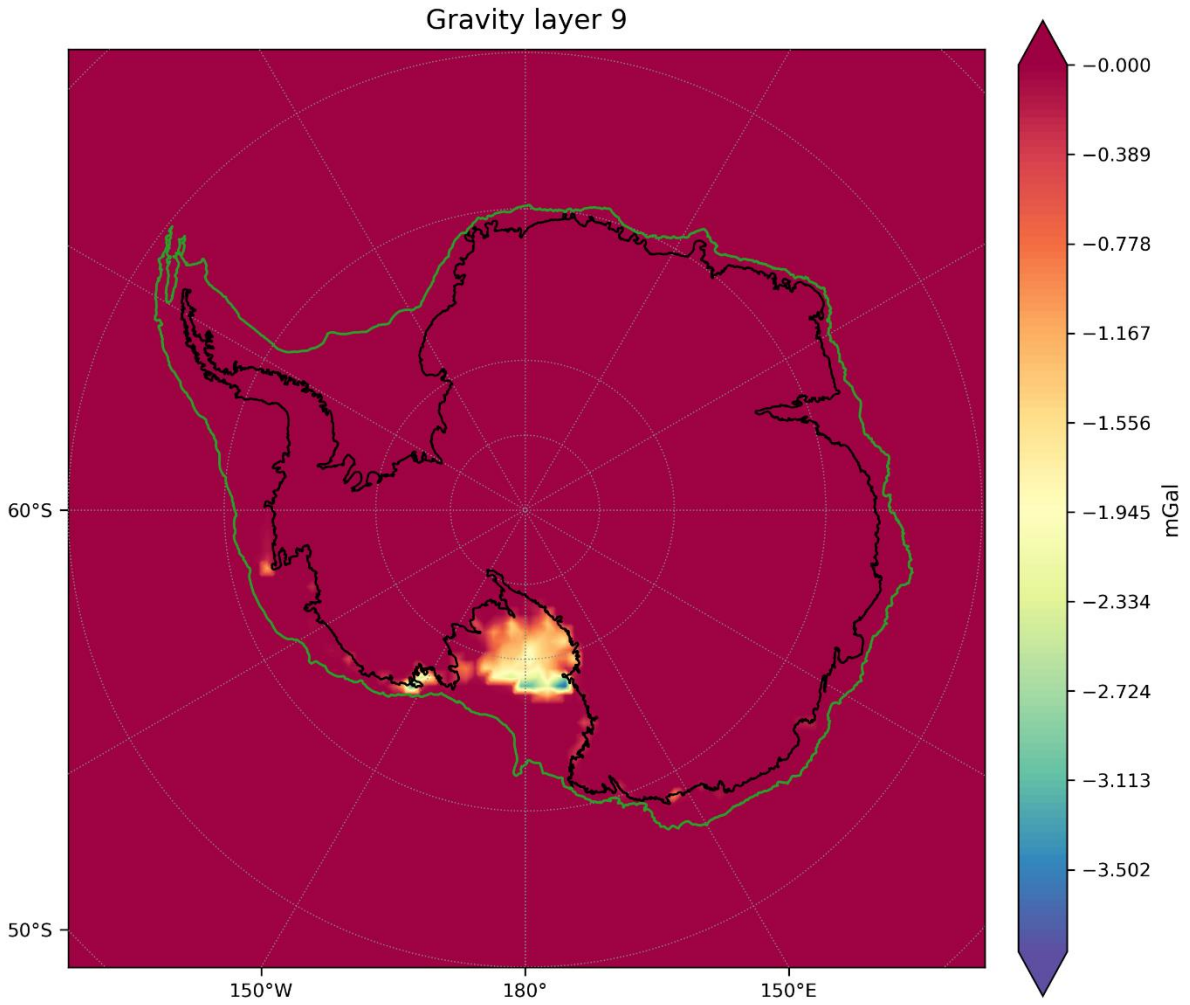

Figure S10: Gravity effect of the layer 9, defined as the layer between the ellipsoid and the ice surface ($-\rho_c$).

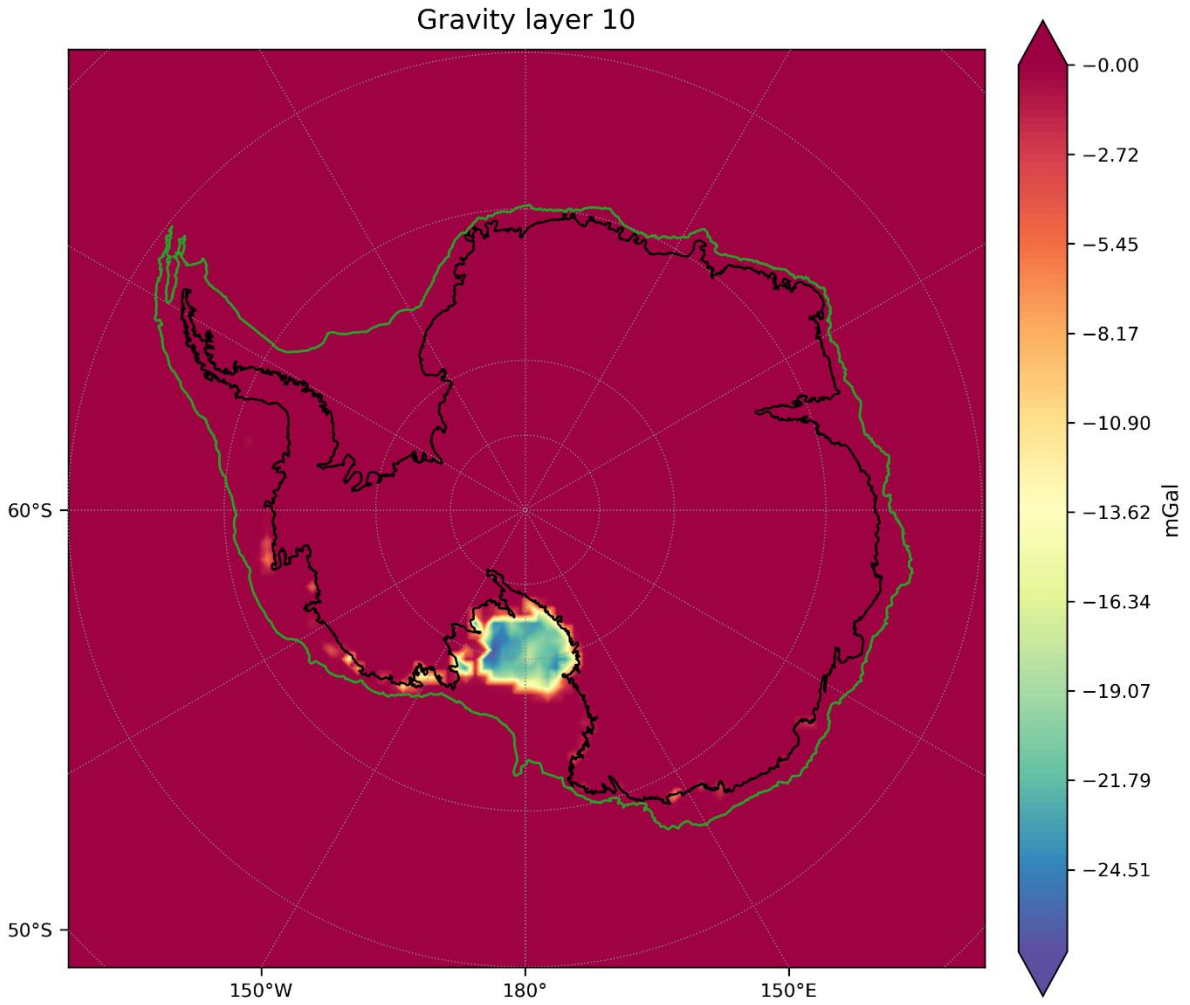

Figure S11: Gravity effect of the layer 10, defined as the ice column (ρ_i − ρ_c).

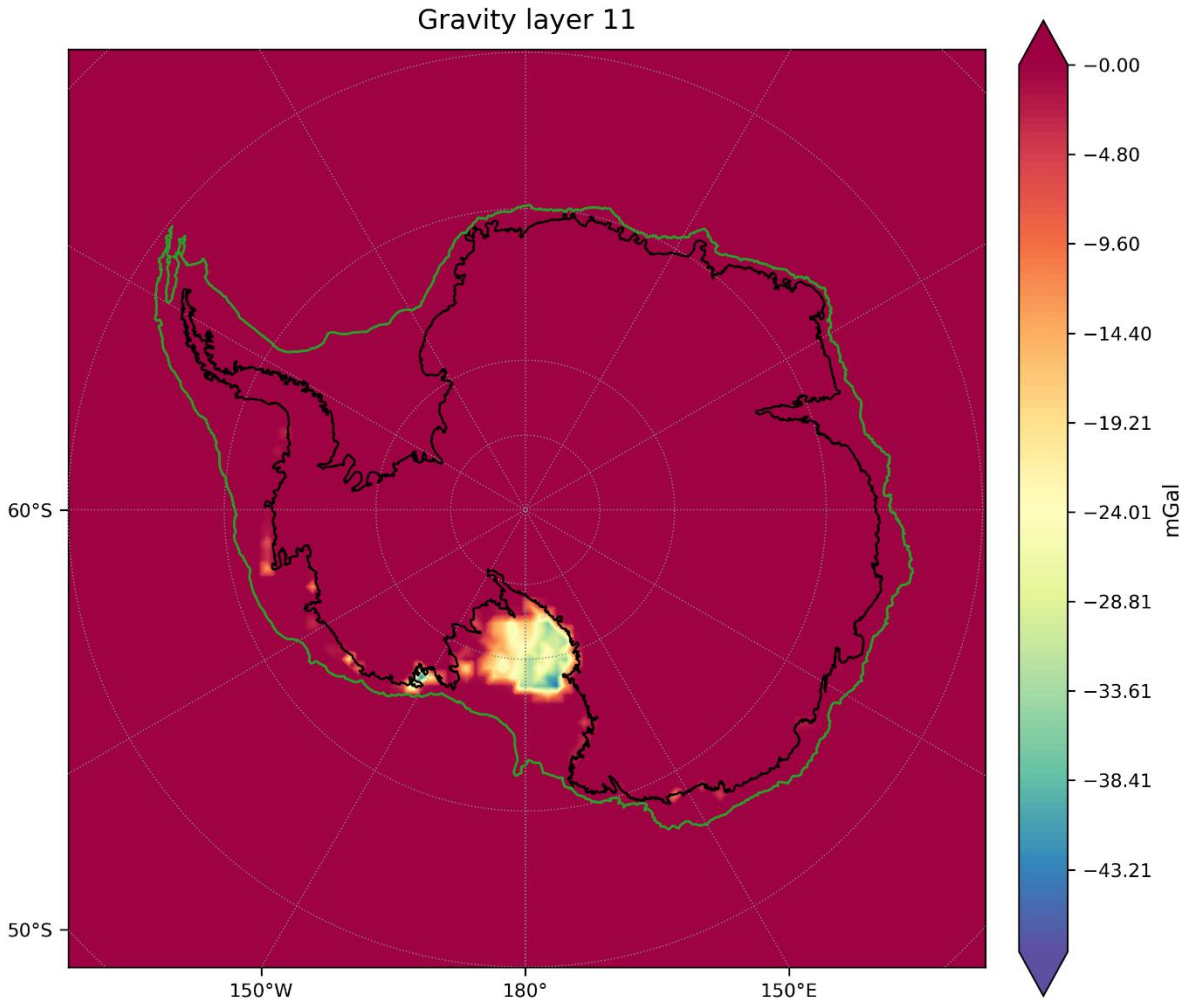

Figure S12: Gravity effect of the layer 11, defined as the water column between the ice base and the seafloor, with density contrast ($\rho_w - \rho_c$).

Section 2: Regression maps containing all data (i.e. without removing the outliers)

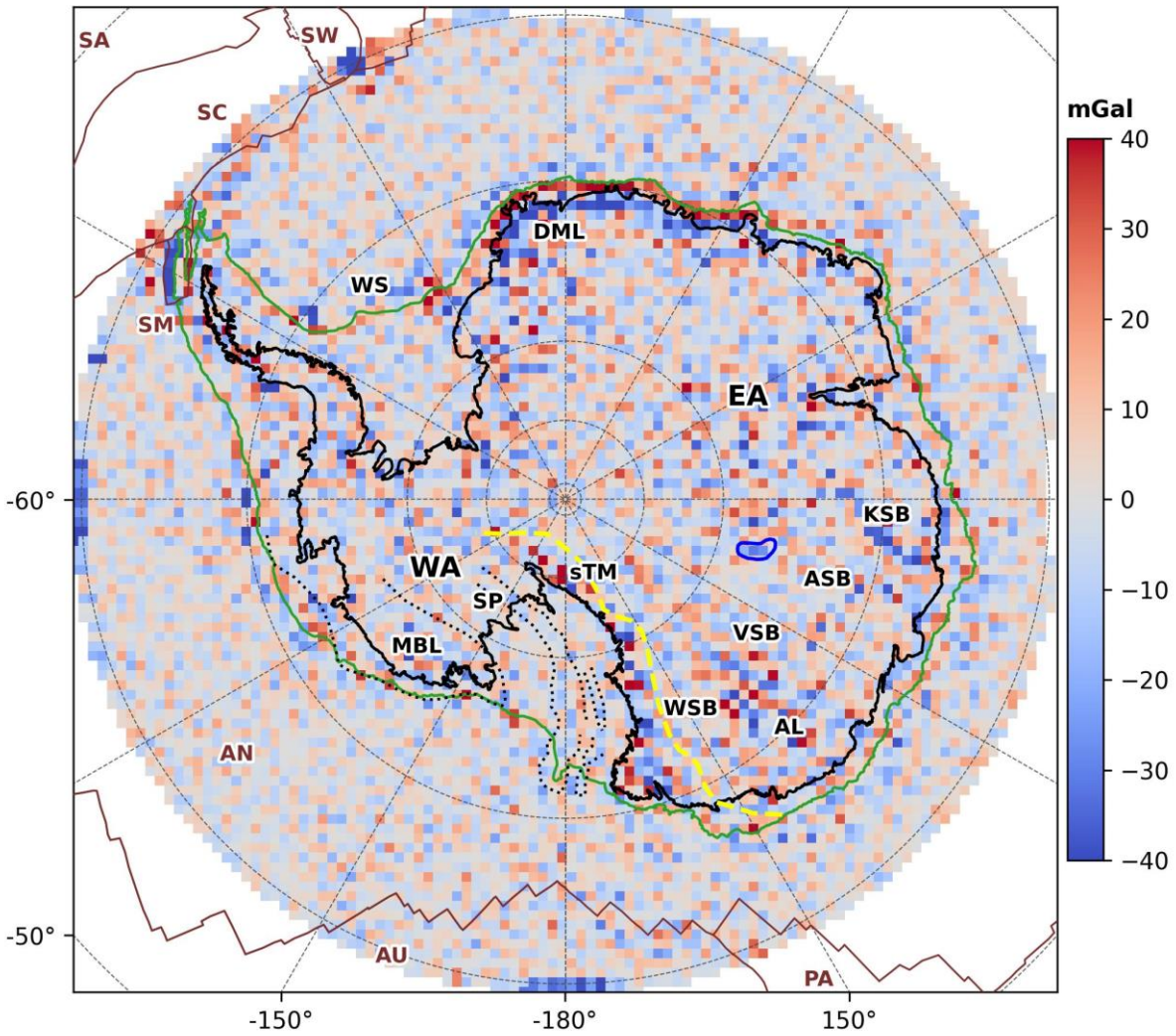

Figure S13: Regression residuals. WA = West Antarctica; EA = East Antarctica. The continental shelf edge (in green) is from Amblas (2018). LV = Lake Vostok (blue polygon); DML = Dronning Maud Land; AL = Adélie Land; KSB = Knox Subglacial Basin; VSB = Vincennes Subglacial Basin; WSB = Wilkes Subglacial basin; MBL = Marie Bird Land; SP = Siple Coast; sTM = Southern Transantarctic Mountains; WS = Weddel Sea. Tectonic plate boundaries from Bird (2003) in brown. SM = Shetland Microplate; PA = Pacific Plate; AN =Antarctic Plate; AU = Australian Plate, SC = Scotia Plate, SW = Sandwich Plate and SA = South American Plate. The Ross Orogen inboard boundary is represented by the dashed yellow line) and the West Antarctic Rift System by the dotted black lines.

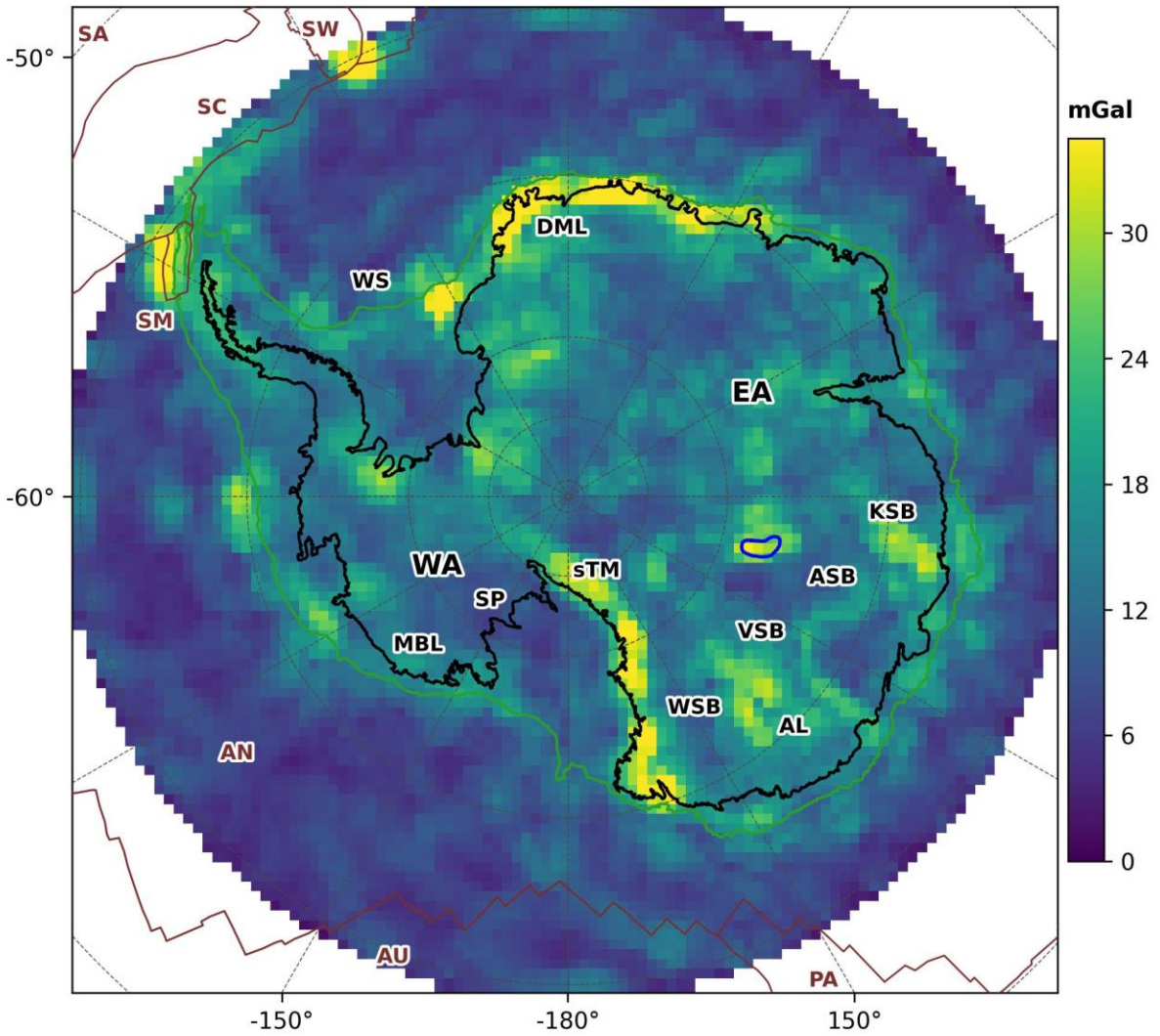

Figure S14: Root Mean Square Error. Abbreviations of geological features are the same as in Fig. S13.

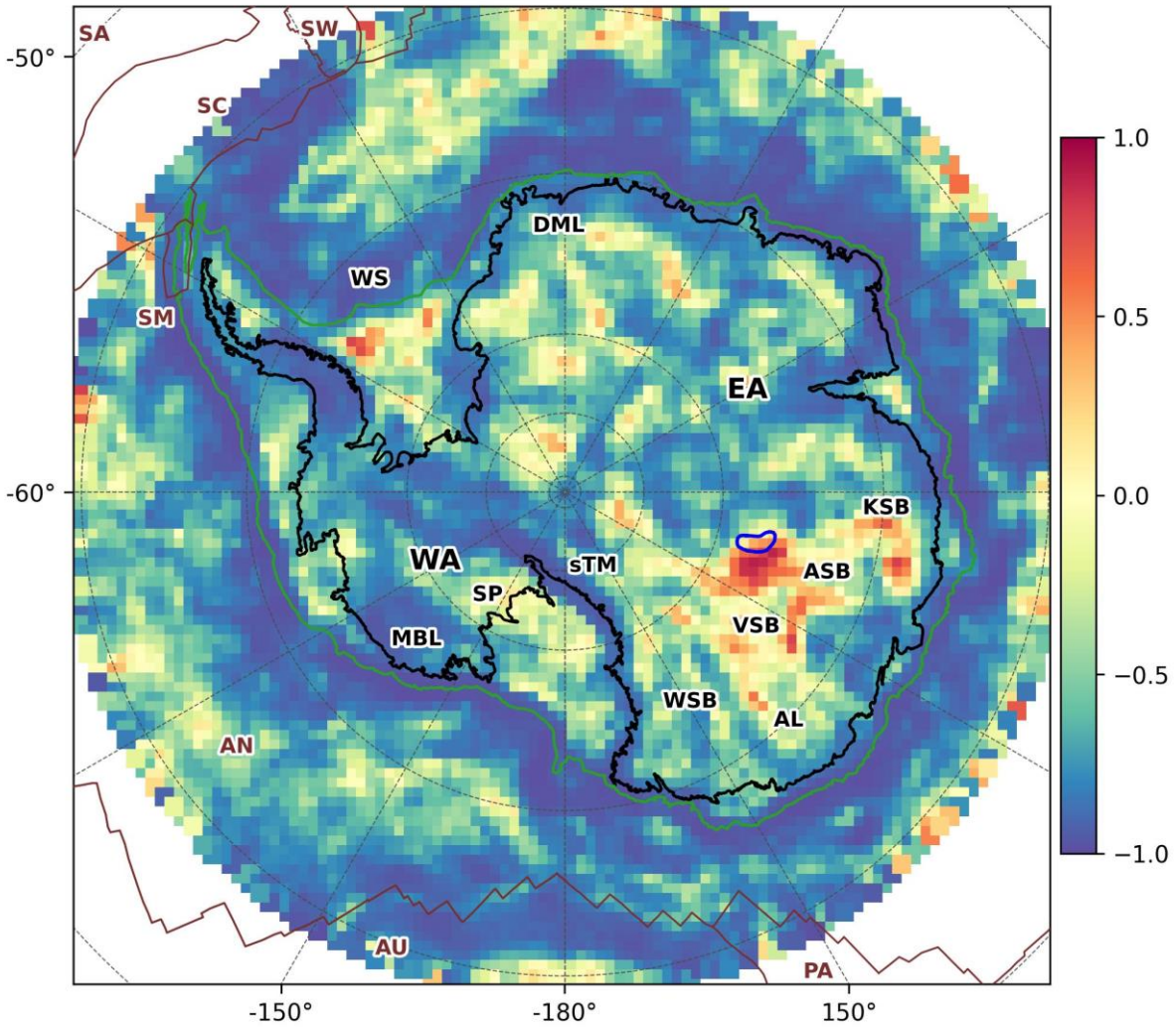

Figure S15. Correlation coefficient between Bouguer anomaly and filtered equivalent topography. Abbreviations of geological features are the same as in Fig. S13.

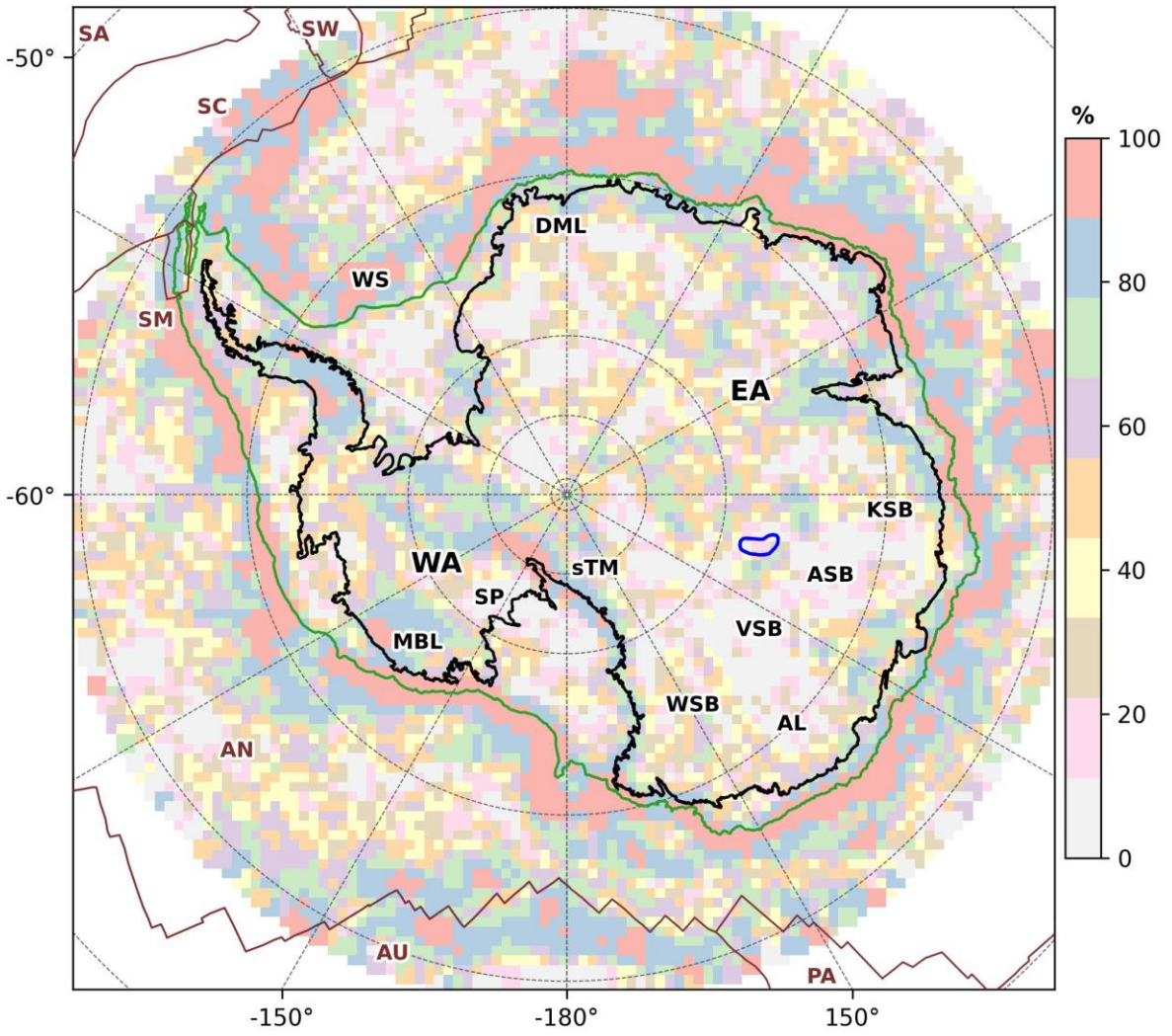

Figure S16. Coefficient of determination (R^2). Abbreviations of geological features are the same as in Fig. S13.

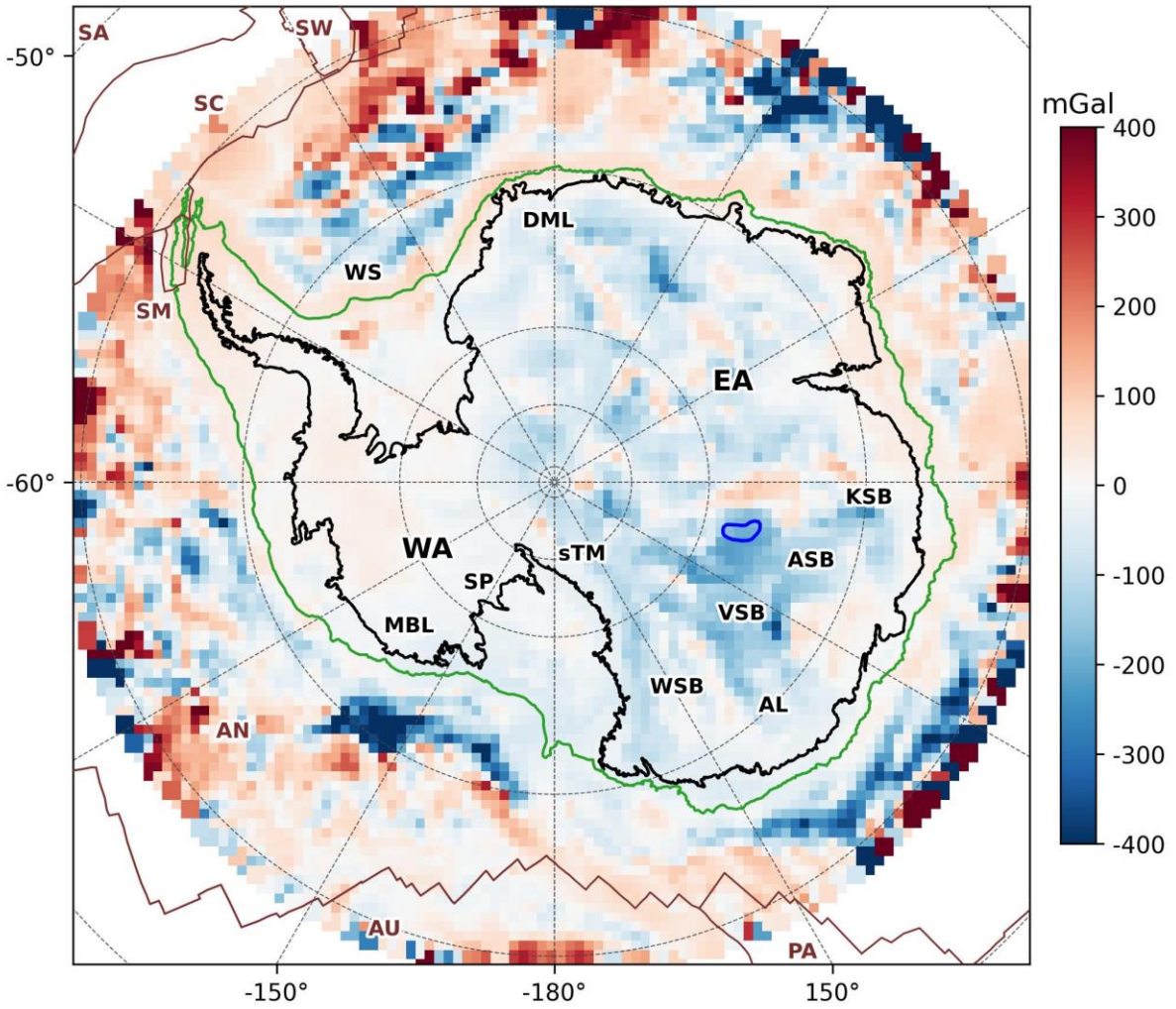

Figure S17. Intercept map showing the spatial distribution of regression intercepts between Bouguer anomaly and filtered topography. Abbreviations of geological features are the same as in Fig. S13.

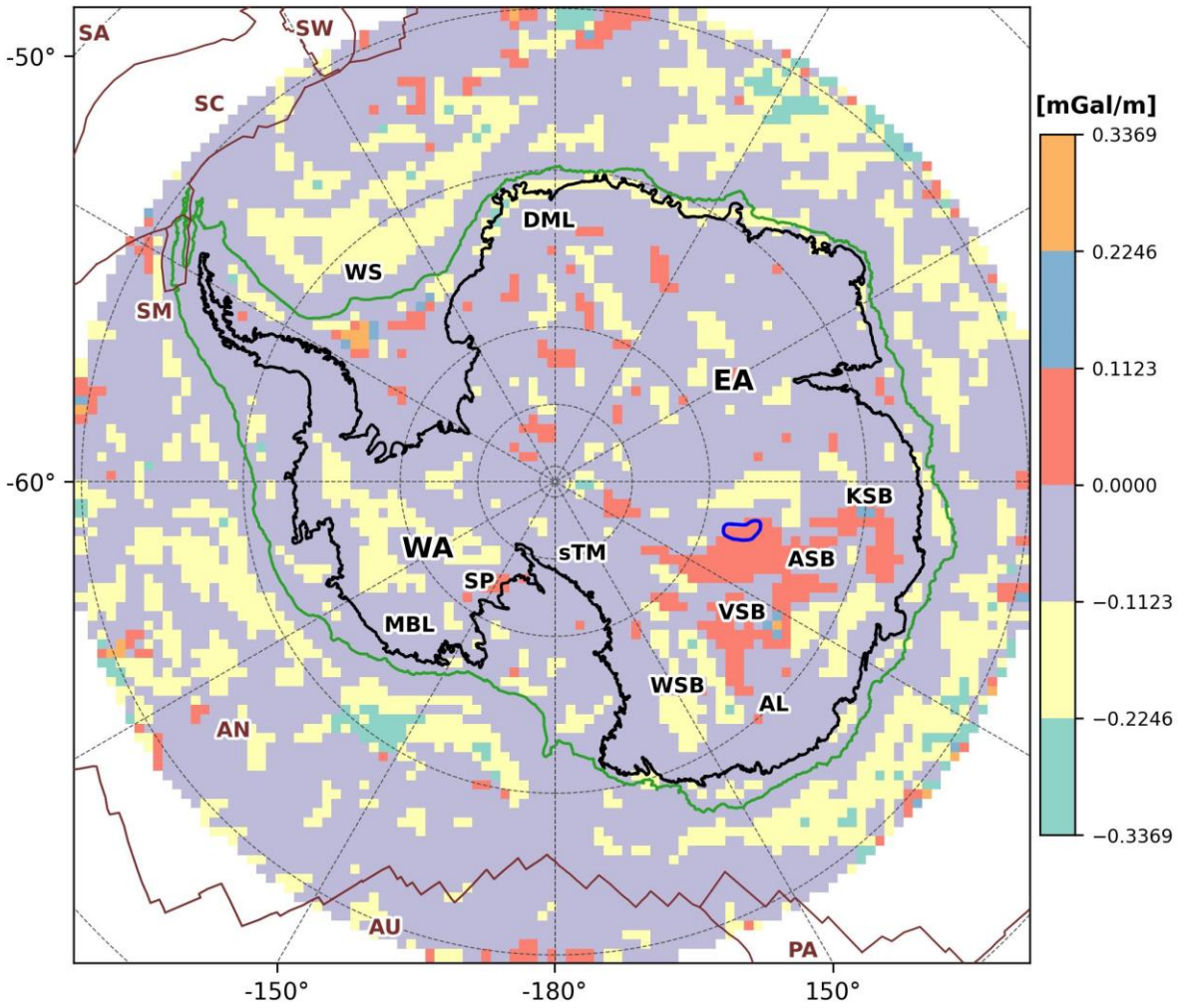

Figure S18. Slope of the regression between Bouguer anomaly and filtered topography, illustrating regional deviations from the theoretical Airy value (−0.1123 mGal m^{-1}). Abbreviations of geological features are the same as in Fig. S13.

Section 3: Regression residuals

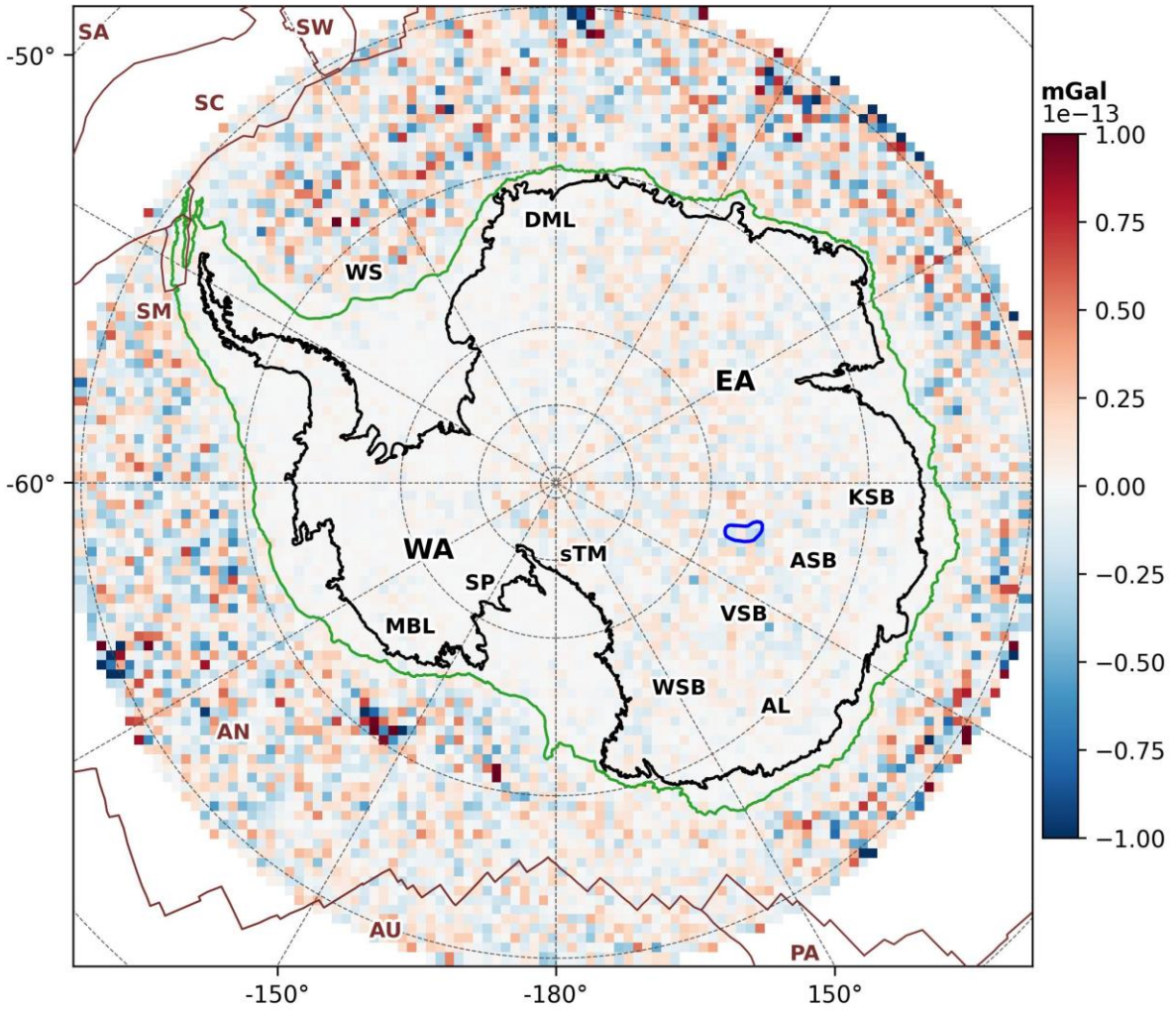

Figure S19. Map of mean residual values associated with each regression. Abbreviations of geological features are the same as in Fig. S13.

Section 4: To facilitate the visualization of the residual calculation procedure, a sequence of schematic illustrations is provided. The figures show how regression parameters, estimated within overlapping circular windows (264 km diameter), are used to compute residuals pointwise within smaller, non-overlapping central tiles (66 × 66 km). The first panels illustrate window displacement along the x and y directions separately, while the final panel presents the

full two-dimensional configuration. In all cases, adjacent windows are shifted by 66 km, resulting in a 75% overlap.

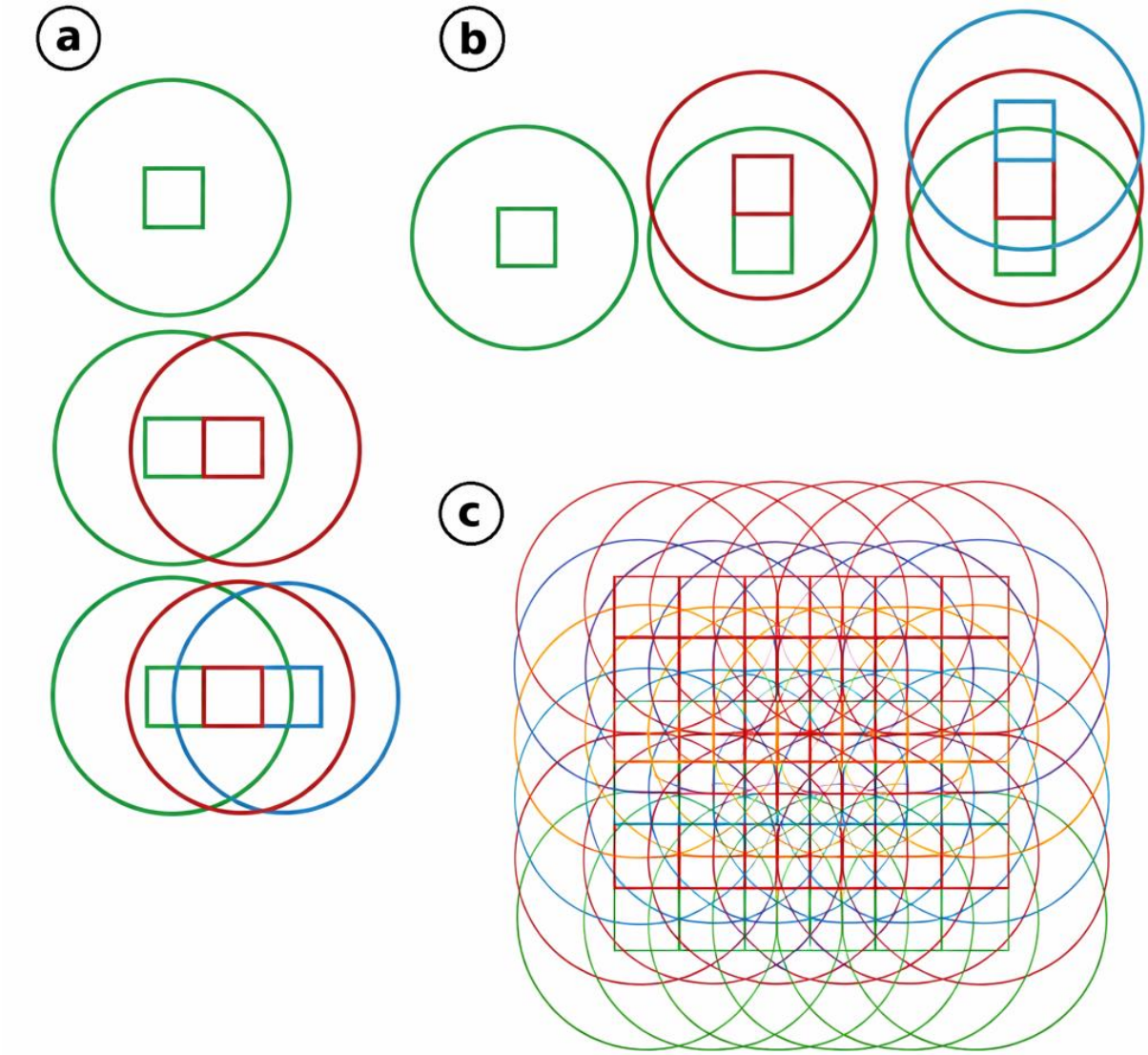

Figure S20: a) Schematic representation of the moving-window procedure used for residual calculation, showing displacement along the x direction. Regression parameters are estimated within circular windows (264 km diameter), which are shifted by 66 km between consecutive positions, resulting in a 75% overlap. Residuals are then evaluated pointwise within the central 66 × 66 km square associated with each window. B) Same as Figure S20 a, but for displacement along the y direction. Circular windows overlap by 75% due to a 66 km step. For each window, residuals are computed pointwise within the corresponding central 66 × 66 km tile. C)Two-dimensional configuration of the moving-window approach used for residual calculation. Circular windows (264 km diameter) are distributed on a regular grid with 66 km spacing, producing a 75% overlap in both directions. Each window provides a set of regression parameters that are used to compute residuals within its central 66 × 66 km tile, resulting in a spatially consistent residual field.

Section 5: ADMAP-2 Magnetic anomaly

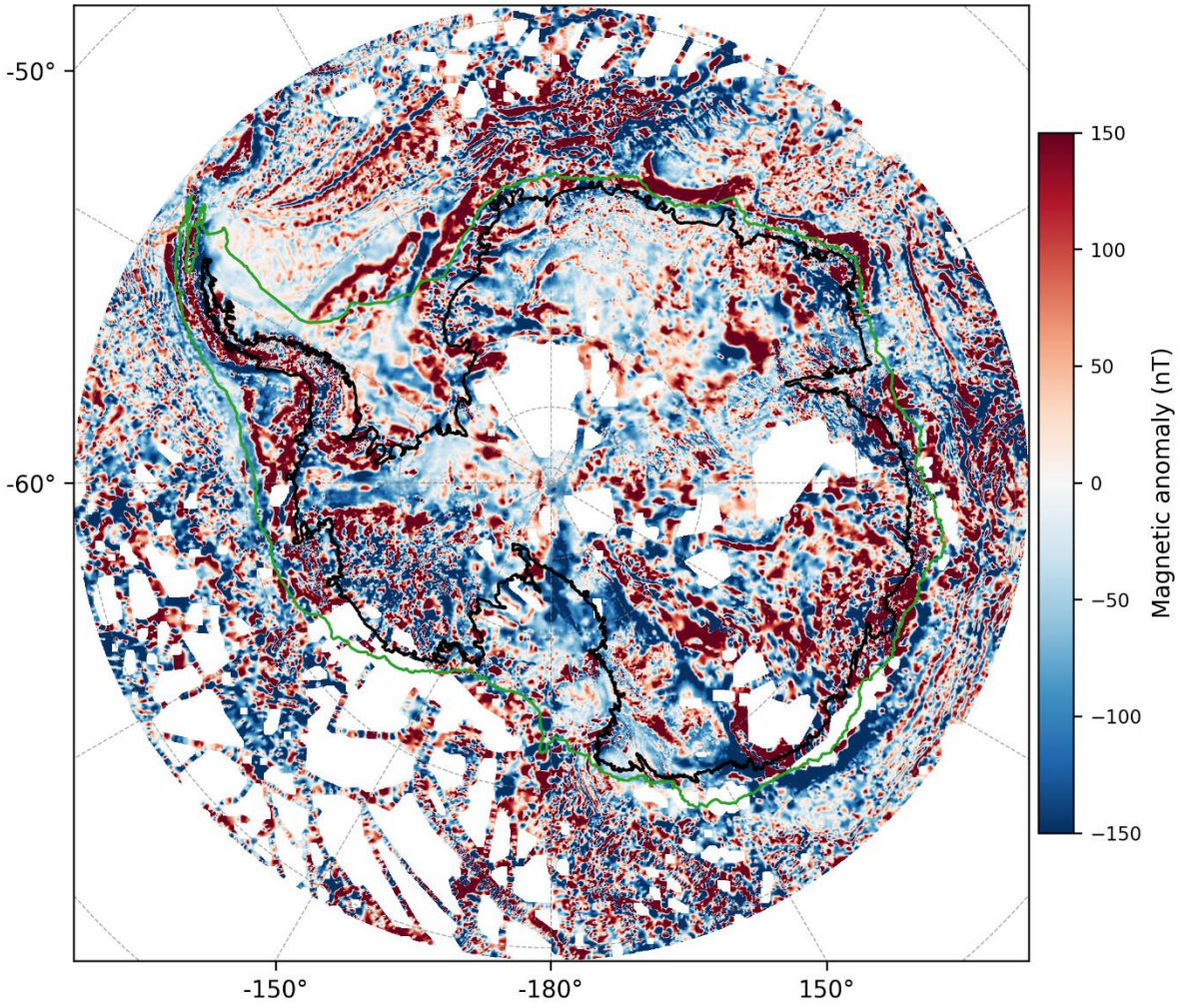

171

172 Figure S21: ADMAP2 dataset (Golynsky et al., 2018).